

5

Confocal Microscopy

Nikolaus Naredi-Rainer, Jens Prescher, Achim Hartschuh, and Don C. Lamb

Department of Chemistry, Ludwig-Maximilians-Universität München, Butenandtstr. 5–13, München 81377, Germany

5.1 Evolution and Limits of Conventional Widefield Microscopy

Conventional widefield fluorescence microscopy (cf. Chapters 1 and 2) captivates the observer with details that it can reveal about the microscopic world with comparatively low technical effort. Scientists have always been striving to find ways to enhance this powerful tool, and significant advances have been achieved. In its long history, Robert Hooke was one of the early pioneers, publishing the seminal book *Micrographia* in 1665, and is considered to be the father of optical microscopy. However, the capacity of Hooke's microscope was limited technically by the quality of the lenses, which was rather poor. A contemporary of Hooke, Antoni van Leeuwenhoek, was an excellent lens grinder and was able to make outstanding lenses with short focal lengths, greatly improving the resolving power of microscopes. The microscopes built by van Leeuwenhoek were constructed using a single lens, and hence they were technically only simple magnifying glasses, but were capable of magnifications of 200–300-fold, allowing some of the first detailed observations of the microscopic world. The investigations of van Leeuwenhoek are still considered exceptional, and from his descriptions and drawings, it is easy to recognize the bacteria (referred to as *animalcules*) or algae that he observed.

The next breakthrough in microscopy occurred 200 years later in 1846 when Carl Zeiss set out to build optical microscopes whose spatial resolution was no longer limited by technology. He joined up with Ernst Abbe, who presented a theoretical derivation of the resolution capacity of an optical microscope. Expanding on an earlier theory by George Airy [1], he showed that diffraction of light on the finite opening of the microscope objective is the most noticeable factor that limits resolution [2]. The diffraction pattern of light focused through an ideal lens with a circular aperture is described by the Airy pattern. Its size depends on the angular aperture α and the refractive index n of the surrounding medium. In this context, he also coined the term *numerical aperture* (NA) defined as $NA = n \sin \alpha$ (cf. Section 2.2.4). Together with Hermann von

Helmholtz, Abbe was able to describe the smallest distance, Δx , at which objects could be separated and still resolved:

$$\Delta x = \frac{\lambda}{2NA} \quad (5.1)$$

where λ is the wavelength of light. Lord Rayleigh later took into account how an ideal point object would be imaged in three-dimensional space. According to Rayleigh's criterion [3], the distance Δx at which two points can just be resolved corresponds to the distance from the center of the Airy pattern to its first minimum (Figure 2.9b):

$$\Delta x = \frac{0.61\lambda}{NA} \quad (5.2)$$

A formal and more detailed approach to the Rayleigh criterion is given in Chapter 2.

Although the Rayleigh criterion is often used in microscopy for estimating the diffraction-limited resolution, the real resolving power of a microscope depends on the image contrast and photon statistics, or, in general, on the signal-to-noise ratio of the measurement. This led the astrophysicist C. M. Sparrow to present another specification for the *resolution limit* (the Sparrow criterion). Two signals are still resolvable until the dip between the two point-spread functions (PSFs), as shown in Figure 2.10c, is no longer detectable [4].

There are several reasons why contrast can be disadvantageously low in widefield microscopy, thus limiting its resolving power. First, assuming that absorption of the sample is negligible, excitation in widefield microscopy is not limited to the focal plane. The resulting image on the detector is not restricted to signals originating from the focal plane. However, points that do not lie in the focal plane of the detector and the objective will be imaged out of focus and their intensity will be dispersed in space, increasing the background signal. Furthermore, especially for biological samples, scattering effects such as the Tyndall effect are very common. This effect describes the scattering of light from particles whose size is comparable to the wavelength of the light. Because of the scattering of light, photons that were originally coming from out-of-focus areas of the sample may be redirected into the focal plane and subsequently contribute to a diffuse background. It is often the low image contrast that limits the spatial resolution rather than pure wave-optics criteria. For this reason, it was obvious that new ways to increase image contrast had to be found in order to broaden the hitherto-existing applications of optical microscopy.

5.2 Theory of Confocal Microscopy

5.2.1 Principle of Confocal Microscopy

In the late 1950s, Marvin Minsky developed confocal microscopy with the aim of being able to perform imaging in dense tissue such as the brain (see Box 5.1). The trick of confocal microscopy is to use two pinholes to restrict the excitation and detection beams and thereby suppress the detection of out-of-focus light.

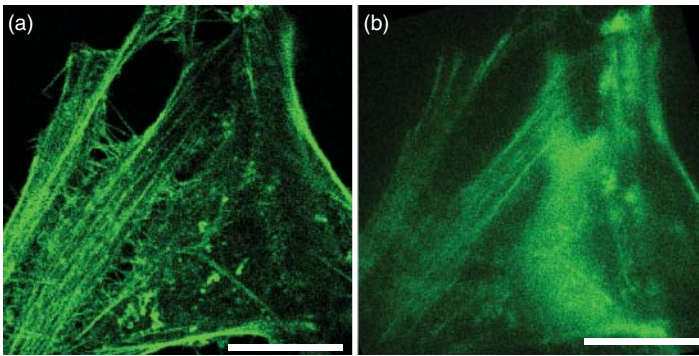
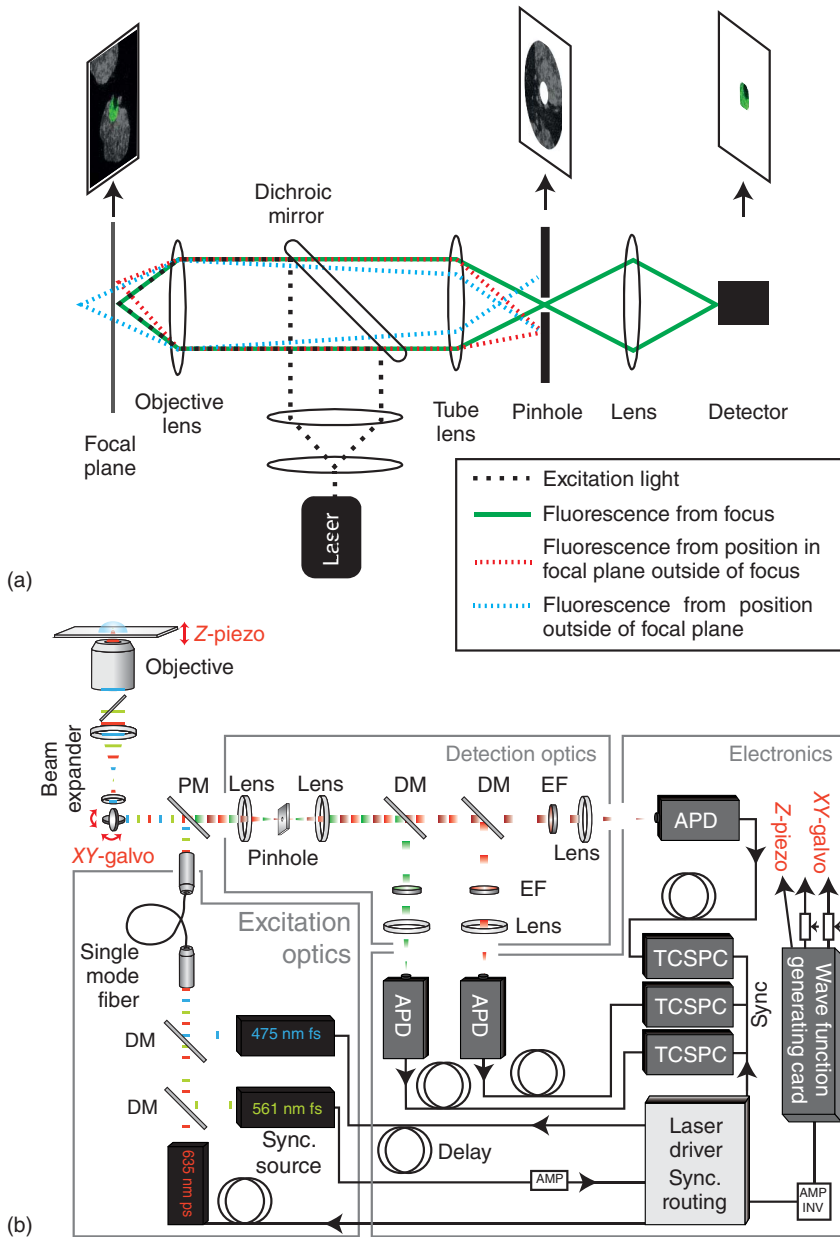


Figure 5.1 Confocal and widefield image of HeLa cell actin filaments. These images demonstrate the capability of confocal microscopy to provide detailed images of cellular structures through the improved axial resolution. The actin filaments of a HeLa cell were stained with Alexa Fluor 647-phalloidin and imaged. (a) On the scanning confocal microscope, actin filaments are clearly visible without blurring from out-of-focus fluorescence. A three-dimensional reconstruction from a confocal z-stack of the cell can be viewed in the online material. (b) The corresponding conventional widefield microscope image is blurred and a high fluorescent background is visible. Scale bars: 20 μm .

The two pinholes are both mounted in image planes of the microscope and are thereby “con”-focal. Figure 5.1 illustrates the sectioning capabilities of confocal microscopy. Actin filaments in HeLa cells were stained with Alexa Fluor 647-labeled phalloidin. The confocal fluorescence image reveals details of complex structures in three dimensions (Figure 5.1a and online supplementary material) that would not be accessible by widefield microscopy (Figure 5.1b). A schematic of the beam paths of a modern confocal microscope is shown in Figure 5.2a. For comparison, we have also included a schematic of one of our home-built confocal microscope setups in Figure 5.2b. Typically, a coherent laser beam is chosen as the excitation source (shown in Figure 5.2a as a dotted

Figure 5.2 Principles of confocal microscopy. (a) Schematic of a simple confocal microscope illustrating the function of the confocal detection pinhole. The excitation beam (dotted line, black) is focused onto a sample, and light originating from the focus will pass through the pinhole and reach the detector (solid line, green), whereas light originating from positions adjacent to the focal spot (dotted line, red) or from a different focal plane will be cut out by the pinhole (dotted line, blue). (b) Example for experimental realization of an advanced laser scanning confocal microscope. In this case, pulsed lasers were chosen as excitation sources rather than the continuous wave lasers that are typically used in confocal microscopy. The lasers are combined using dichroic mirrors (DMs). In this setup, one of the lasers also serves as a master clock to synchronize the entire system. The excitation light is guided through a single-mode fiber toward the microscope objective, with an XY galvo mirror system being used for laser scanning. The fluorescence is collected by the same objective, de-scanned by the galvo mirrors, and separated from excitation light by a polychroic mirror (PM). After passing through the confocal pinhole, the fluorescence is separated by color using DMs. The spectra are subsequently cleaned up by the appropriate emission filters (EFs). Avalanche photodiodes (APDs) were chosen as detectors to collect fluorescence photons. Photon counts are registered subsequently by time-correlated single-photon counting (TCSPC) electronics.



black line), in which case an excitation pinhole is no longer necessary. The excitation beam, expanded by a set of lenses, is subsequently reflected by a dichroic mirror that splits the excitation light from the fluorescence signal (shown as a solid green line) based upon their different wavelengths (cf. Section 3.4.3). Fluorescence light is collected with the same objective lens and transmitted through the dichroic mirror. To ensure that only light from a small

region of the sample reaches the detector, a pinhole is placed in the image plane of the sample.

The confocal detection pinhole defines what light reaches the detector: Fluorescence photons originating from the focus of the excitation beam pass through the pinhole and are detected (green line, Figure 5.2a). Out-of-focus light (or in other words, light that is not confocal with the pinhole) is blocked by the pinhole. For example, the blue line in Figure 5.2a depicts the path of photons coming from a different axial plane of the sample. This light is focused at a different position within the microscope and is out of focus with respect to the plane of the pinhole. Hence, the vast majority of light will be blocked by the pinhole. Likewise, background light coming from the focal plane but displaced laterally from the position of the pinhole in the sample plane (red line, Figure 5.2a) will also be blocked. Although less light reaches the detector, the confocal pinhole leads to a significant improvement in the signal-to-noise ratio of the collected image compared to bright-field methods. As only photons emitted from the focal plane are detected, it is possible to detect an optical slice of the sample, as illustrated by the example of a confocal image of a cell depicted above the beam path in Figure 5.2a. As we will see in the more mathematical discussion in the following section, the major impact of the pinhole under normal conditions is in generating *z*-resolution with little influence on the lateral resolution.

After the pinhole, the remaining light beam can be directed immediately onto a detector, which might be a photomultiplier tube (PMT), an avalanche photodiode (APD), or, in some cases, also a charge-coupled device (CCD) camera as is the case for a spinning disk confocal microscope (SDCM). Further information about detectors for confocal microscopy can be found in the information box about instrumentation. It is also possible to introduce further optical elements into the beam path after the pinhole. For example, a single lens can be used, as depicted in Figure 5.2a, to image the pinhole on the detector surface. It is also possible to include additional optics such as a polarizing beam splitter or a dichroic mirror. In these cases, it is recommended to first recollimate the light transmitted by the pinhole before mounting the additional optics and then focusing the detection beam on the respective detectors.

A second aspect of confocal microscopy that is important for imaging is scanning. The detection volume in confocal microscopy is typically diffraction-limited. Hence, an entire image cannot be recorded at the same time, as is the case in widefield microscopy. To gain spatial information, either the sample is moved with respect to a stationary optical path or the laser beam is scanned over the sample. More details regarding different confocal laser scanning methods are given in Section 5.2.3.

Box 5.1 A Brief History of the Development of Confocal Microscopy

A new breakthrough to enhance the capability of optical microscopes occurred in the late 1950s with the development of a new type of microscope by the American mathematician Marvin Minsky, which is nowadays known as the

(Continued)

Box 5.1 (Continued)

confocal microscope. Minsky is more known for his numerous and seminal works on artificial intelligence, which led him to think about ways of improving optical microscopy. His original intention was to study the functioning of the human brain. He realized that optical measurements in this relatively dense tissue were very difficult with conventional light microscopes owing to the high background in the images. In order to solve this problem, he developed a new microscope that used a pinhole to block all light that did not come from the focal region. The sample was then scanned, point by point, instead of illuminating the whole sample at once as in widefield microscopy. In 1958, Minsky was able to present a first prototype for a confocal microscope. A sketch of this prototype is shown in Figure 5.3, taken from the patent that was granted to him for his invention in 1961 [5].

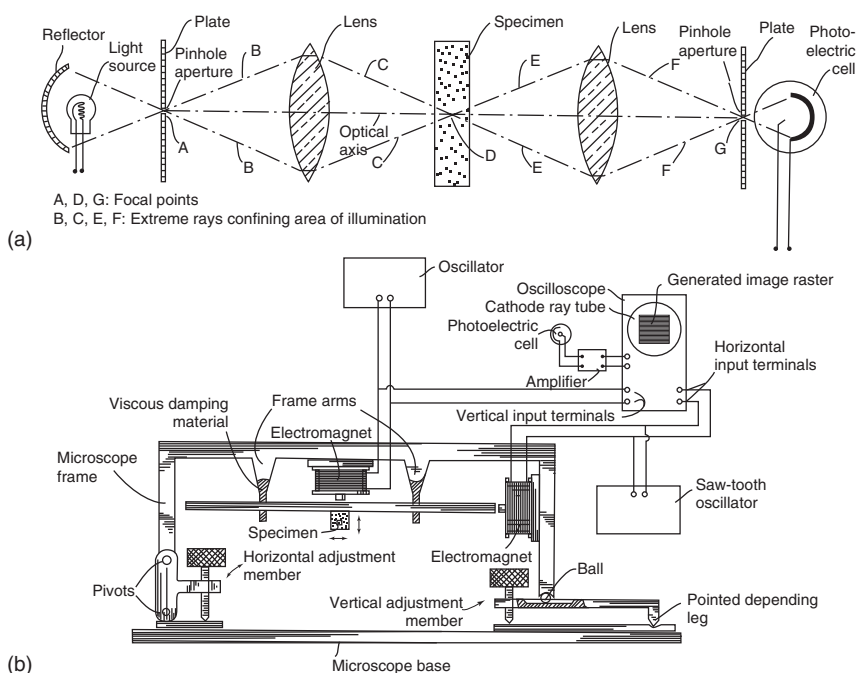


Figure 5.3 The confocal microscope prototype developed by Marvin Minsky. (a) Optical beam path of a confocal microscope. (b) Schematic of the scanner proposed for sample scanning with the prototype confocal microscope. (Source: After Minsky 1961 [5].)

Although Minsky receives all the credit for the development of the confocal microscope, it should be mentioned that a non-imaging scanning confocal microscope was built by the Japanese scientist Naora in 1951 [6] to perform spectroscopic studies on nucleic acids. In contrast to Minsky's version, this system was only designed to measure spectra and did not provide any images of the sample.

In the years shortly after the invention of the confocal microscope, the device had minimal success, which can be largely attributed to the limited technical equipment available at that time and forced the early pioneers to accept several compromises. First, a high-intensity light source was needed, and lasers were not known in 1958. The best light sources that were available were carbon arc lamps, but these lamps required high maintenance. Therefore, Minsky decided to use zirconium-arc lamps that represented the second best alternative. The second compromise was between scanning performance and the pixel dwell time. Minsky decided to move the sample itself in order to achieve higher optical stability, with the disadvantage of a relatively slow scan speed. Detection of the resulting signals was done using PMTs whose output was made visible on the screen of a long-persistence radio oscilloscope. This method had the advantage that a complete image of the sample could be visualized at once, although it could be kept on the screen of the oscilloscope for only about 10 s. Furthermore, to obtain the entire image on the screen, very short dwell times had to be accepted owing to the relatively slow scanning process, which consequently meant a decrease in image quality. When looking back, Minsky said, *...it occurs to me that this concern for real-time speed may have been what delayed the use of that scheme for almost thirty years* [7]. Had he accepted slower data acquisitions rates and recorded the resulting picture point by point on a film, his new method may have been more successful.

In the decades that followed, several technical advancements helped confocal microscopy to obtain more and more acceptance in the scientific community. Here, especially the invention of the lasers in the 1960s has to be mentioned, which offered a bundled, intense, monochromatic, and coherent light source that was able to efficiently excite fluorescent samples. Another important advancement in this context was the development of the first dichroic mirrors in 1967 [8]. With the help of this technical masterpiece, it became much easier to effectively separate excitation and detection pathways, which allowed confocal fluorescence microscopy to be performed with a single objective.

The next challenge was improving the scanning process (cf. also Section 5.2.3.2). Using the so-called galvanic mirrors (a variation of classic galvanometer where a mirror can be moved by an electric current), the excitation and detection beam could be scanned over the sample very accurately. A second approach, the so-called SDCM (cf. Section 5.2.3.3), was first presented by Egger and Petran in 1967 [9]. They used an array of pinholes placed on a spinning disk, making it possible to scan several points of the image simultaneously. Thus, they were able to scan in real time. After this first practical application of confocal microscopy, another 20 years of steady progress was necessary before the technique became accepted as the gold standard for microscopy. Two key publications in 1987 finally led to the acceptance of confocal microscopy. In the first work, White *et al.* [10] used confocal microscopy to image various elements of cells and larger tissues. They were able to demonstrate the considerable improvement in contrast and resolution compared to conventional microscopy. In the second work, Meer *et al.* [11] showed that it was not only possible to study structures in fixed cells,

(Continued)

Box 5.1 (Continued)

as in White's work, but that confocal microscopy is also a suitable tool to observe dynamic processes in living cells, which they demonstrated by following the pathway of sphingolipids in epithelial cells.

Box 5.2 Instrumentation

In general, both continuous wave (CW) and pulsed lasers can be used in a confocal setup. CW lasers are used in most conventional confocal microscopes. However, the use of sub-nanosecond pulsed lasers brings an additional dimension into play and makes it possible, for example, to determine the fluorescence lifetime and thereby perform fluorescence lifetime imaging microscopy (FLIM) (see Chapter 13) in addition to performing confocal imaging. The disadvantage of pulsed lasers is that they may lead to enhanced photophysics in fluorescent dyes, as the photon flux and thereby the energy density during the laser pulse is higher than for CW lasers. In contrast, CW lasers are more suited for applications where an extremely stable flux of photons over a wide range of timescales is needed (e.g., nanosecond fluorescence correlation spectroscopy (FCS) and rotational FCS).

Detectors should be chosen based on the details of the measurement. First, one has to decide whether a widefield detector or a point detector is desired. Wide-field detectors such as scientific complementary metal-oxide-semiconductor (sCMOS) or electron multiplying CCD (EMCCD) cameras offer high sensitivity and are suitable for applications such as spinning disk confocal microscopy (see Section 5.2.3.3). For laser scanning applications, a single point detector such as PMTs or APDs are typically the better option (see Section 5.2.3.2). PMTs have the advantage of a very short response time – the so-called instrument response function (IRF) – when operated in single-photon counting mode and hence are well suited for fluorescence lifetime measurements. They also have a large dynamic range and can be used to measure bright samples. However, they typically have low sensitivity and suffer from high dark count when they are not cooled. APDs, on the other hand, offer very low dark counts (down to <10 Hz) and high sensitivity, but they usually have a broader IRF, and the maximum count rates are limited to ~10 MHz. Hence, they are well suited for low-light-level experiments where high sensitivity is desired.

Detectors can be run in either analog or digital mode. The technical difference occurs after the photosensitive electronics. The electrical pulses are either integrated over a certain time by an *integrator* in analog mode or digitalized by a *discriminator*. In the first case, the output voltage is proportional to the number of incoming photons. In the second case, each detected photon is converted into a transistor-to-transistor logic (TTL) pulse, which can be recorded by a counting card or a time-correlated single photon counting (TCSPC) card. Analog detection is advantageous for bright samples, whereas digital detection is better when more information from a limited number of photons is needed.

5.2.2 Radial and Axial Resolution and the Impact of the Pinhole Size

In confocal microscopy, the pinhole is the key element that provides the improved resolution and sectioning capabilities of the instrument. For a deeper understanding of the method, it is important to briefly discuss the details of image formation and the influence of the pinhole.

The intensity distribution for a point-like object imaged using ideal lenses (i.e., only the effect of diffraction is considered, the lenses are assumed to produce no chromatic or spherical aberrations) is given by the Airy pattern. Mathematically, the Airy pattern is the square modulus of the Fourier transform of an aperture:

$$I(r) = I_0 \left[\frac{2J_1(2\pi r \text{ NA}/\lambda_0)}{2\pi r \text{ NA}/\lambda_0} \right]^2 \quad (5.3)$$

where J_1 is the first-order Bessel function of the first kind. The *resolution of a system* is defined as the minimum distance at which two point-like objects can still be resolved. Using Rayleigh's criterion, the minimum *lateral* resolution r_{lateral} obtainable with ideal lenses is given by

$$r_{\text{lateral}} = 1.22 \frac{\lambda_0}{\text{NA}_{\text{Objective}} + \text{NA}_{\text{Condensor}}} \quad (5.4)$$

where the value of 1.22 comes from the first zero of the Bessel function in the Airy pattern, λ_0 is the wavelength of light in vacuum, and $\text{NA}_{\text{Objective}}$ and $\text{NA}_{\text{Condensor}}$ are the numerical apertures of the objective and the condenser, respectively. Often, the NA of the objective and the NA of condenser lenses are matched, or measurements are performed using epi-fluorescence (i.e., the same objective is used for illumination and detection). In these cases, Eq. (5.4) reduces to

$$r_{\text{lateral}} = 0.61 \frac{\lambda_0}{\text{NA}_{\text{Objective}}} \quad (5.5)$$

where r_{lateral} is the distance of the maximum of the Airy pattern to the first minimum. This radius of the Airy disk in the plane of the pinhole can be calculated by multiplying the result from Eq. (5.5) with the total magnification of the instrument. The diameter d ($=2r_{\text{lateral}}$) is referred to as 1 Airy unit (AU). The relationship between Airy unit and the full-width at half-maximum (FWHM) of the Airy pattern is given by

$$\text{FWHM}_{\text{lateral}} = \frac{0.51}{1.22} \text{AU}, \quad \text{where } \text{AU} = 2 r_{\text{lateral}} = 1.22 \frac{\lambda_0}{\text{NA}_{\text{Objective}}} \quad (5.6)$$

It is important to note that Eq. (5.4) and its derivatives are based on the paraxial approximation (i.e., the parts of the electromagnetic field propagating in x - y plane are assumed to be small compared to those propagating in the z -direction). Fortunately, Novotny and Hecht [12] could show that the paraxial approximation delivers surprisingly good results even for high-NA objectives. Otherwise, a full vectorial description of the electromagnetic field would be required for the discussion of high-NA optics.

Until now, we have only considered the effect of diffraction from the aperture of lenses on the formed image. In a confocal microscope, the excitation light is first focused on the sample, and the resulting fluorescence is collected via the objective and guided through the pinhole to the detector. To calculate the optical resolution of the confocal microscope, the effect of diffraction on both the excitation and emission beam paths needs to be considered. In terms of the PSF introduced in Chapter 2, the total PSF in confocal microscopy can be approximated for small pinholes ($d \leq 0.5$ AU) by the product of the excitation and detection PSFs:

$$\text{PSF}_{\text{confocal}} \approx \text{PSF}_{\text{excitation}} \cdot \text{PSF}_{\text{detection}} \quad (5.7)$$

For large pinholes, the Airy pattern of the detection PSF has to be convoluted with the transfer function of the pinhole. This means that the total confocal PSF is the product of the detection PSF, integrated over the transfer function of the pinhole, with the excitation PSF. This is mathematically equivalent to convoluting the excitation and detection PSFs and multiplying the convolution with the transfer function of the pinhole [13]. The effect of the pinhole is illustrated in one dimension in Figure 5.4.

The radial dependence of the Airy pattern can be well approximated by a Gaussian function. The intensity distribution $I(r)$ of a Gaussian in one dimension is given by

$$I(r) = I_0 * e^{-\frac{(r-r_0)^2}{2\sigma^2}} \quad (5.8)$$

where r_0 is the center of the Gaussian peak, σ its standard deviation, and I_0 the amplitude. When using epi-fluorescence, the size of the excitation and detection

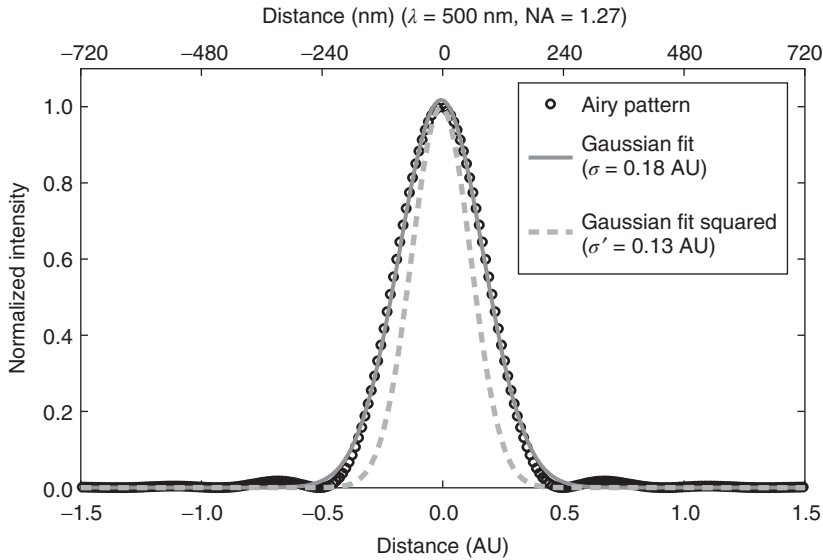


Figure 5.4 PSF and Gaussian approximation. The PSF is represented by black dots, and the Gaussian fit by the solid gray line. The dashed gray line represents the squared Gaussian function and depicts the increased resolution of $\sqrt{2}$ of a confocal microscope when compared to a conventional widefield microscope.

PSFs are equal ($I_{\text{Exc}}(r) = I_{\text{Det}}(r) = I(r)$). The total PSF is given by the product of the two Gaussian functions, which is itself a Gaussian function:

$$I'(r) = I_{\text{Exc}}(r) * I_{\text{Det}}(r) = I_0^2 * e^{-\frac{(r-r_0)^2}{2(\sigma')^2}} \text{ with } \sigma' = \frac{\sigma}{\sqrt{2}} \quad (5.9)$$

The standard deviation (and also the FWHM) of the resulting Gaussian is reduced by a factor $\sqrt{2}$, leading to an increased lateral resolution of a confocal microscope by $\sqrt{2}$:

$$\Delta r_{\text{confocal}} = \frac{1}{\sqrt{2}} * \Delta r_{\text{widefield}} = 0.43 \frac{\lambda_0}{\text{NA}_{\text{Objective}}} \quad (5.10)$$

Assuming equal excitation and detection PSFs, the full three-dimensional confocal PSF is shown in Figure 5.5.

The size of the pinhole can be varied to modify the resolution or increase the light throughput. The axial and lateral FWHM, as well as the fraction of light detected from a point source in the focus of the microscope, are plotted as a function of the pinhole size in Figure 5.6. The excitation and detection PSFs were calculated for an objective with an NA of 0.5, magnification of 60 \times , and an excitation wavelength of 500 nm using Eq. (4.44) from Novotny and Hecht [12]. For a pinhole size of diameter ~ 1 AU, the detection yield reaches a plateau. A plateau is observed when the size of the pinhole is equal to a minimum of the Airy pattern. As there is no intensity at the minima of the PSF, a small variation in the size of the pinhole does not lead to a change in the measured intensity. For a pinhole size of ~ 1 AU, 86% of the light collected from a point-like source passes through the pinhole. The *lateral* resolution determined by the detection PSF then approaches that achieved by widefield detection, but the pinhole still has an impact on the axial resolution. For most applications in confocal microscopy, a pinhole size between 0.8 and 1.0 AU is optimal.

Selecting a pinhole size significantly smaller than 1 AU (typically with diameter ≤ 0.25 AU) leads to an increase in both *lateral* and *axial* resolution. In this case, the *lateral* resolution can be improved by a factor of 1.4 compared to Eq. (5.6):

$$\text{FWHM}_{\text{lateral}} = 0.37 \frac{\lambda_0}{\text{NA}_{\text{Objective}}} \quad (5.11)$$

However, the increase in resolution comes at a significant cost in the intensity. For a pinhole size of 0.25 AU, only $\sim 20\%$ of the collected photons pass through the pinhole. Increasing the size of the pinhole beyond ~ 1 AU does not significantly change the *lateral* resolution, as it becomes dominated by the excitation PSF.

In contrast, the optical thickness is sensitive to pinhole size and becomes very important when measuring real objects. The optical thickness in widefield microscopy is not defined by the optical elements but by the thickness of the sample itself. Sharp images of biological objects can be generated if the specimen itself is sufficiently thin; otherwise, the sharp image of the focal plane is blurred due to out-of-focus light. In confocal microscopy, the optical thickness is determined by the size of the pinhole and the product of the *excitation* and *detection* PSFs. The depth of the *detection* PSF is a result of the diffraction pattern for the emitted light and the geometric-optical impact of the pinhole

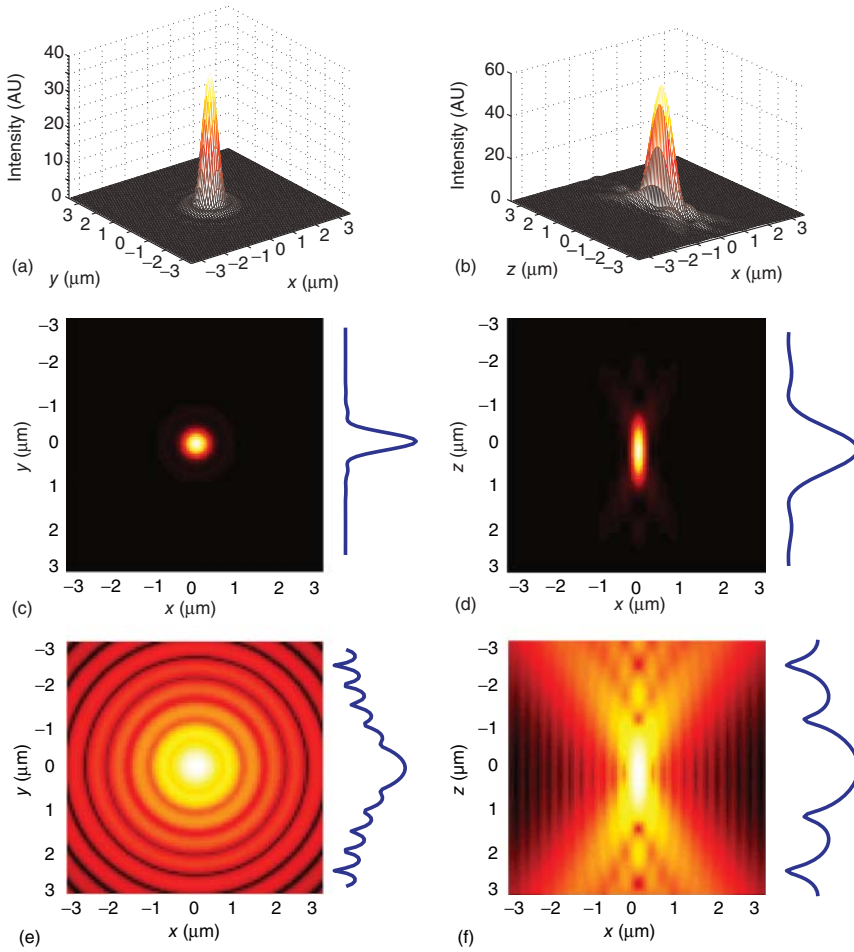


Figure 5.5 Airy pattern resulting from a luminescent point light source. (a, b) 3D representation of the (a) lateral and (b) axial dimensions of the PSF. (c–f) Projections of the intensities of the whole focus onto the x–y and x–z planes, respectively, (c, d) in linear scale, and (e, f) in logarithmic scale. Cross sections through the middle of the displayed PSF are shown on the plots to the right of the images.

[14]. The axial FWHM of the detection PSF is given by:

$$\text{FWHM}_{\text{det;axial}} = \sqrt{\left(\frac{0.88\lambda_0}{n - \sqrt{n^2 - \text{NA}^2}}\right)^2 + \left(\frac{\sqrt{2}n\text{PH}}{\text{NA}}\right)^2} \quad (5.12)$$

where PH is the absolute size of the pinhole in micrometers in the object space. The first squared term under the square root, often called the *wave-optical term*, is constant as long as the objective and the excitation wavelength remain the same. The second squared term under the square root, the *geometric-optical term*, depends on the pinhole size. As the size of the pinhole increases, the

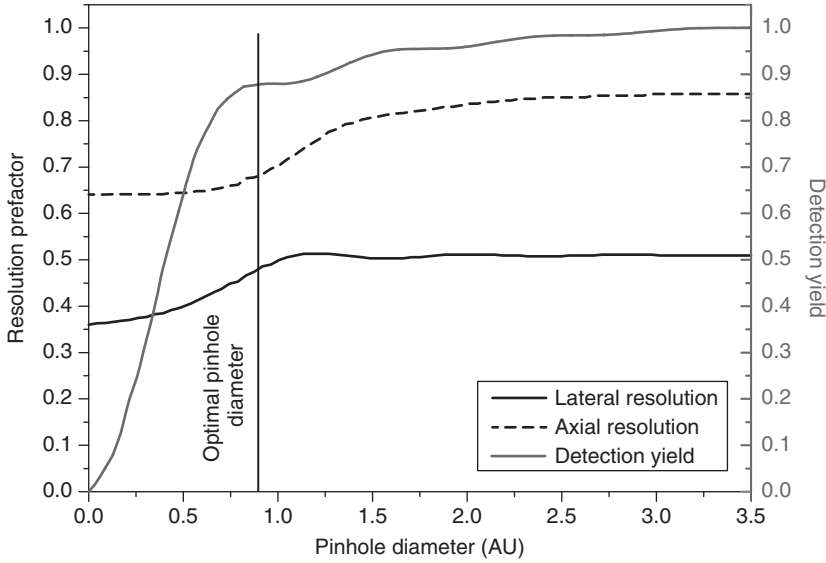


Figure 5.6 Resolution and signal throughput as a function of pinhole size. The solid and dashed black lines show how the resolution prefactor (i.e., resolution in units of $\lambda_0/\text{NA}_{\text{Objective}}$) changes for lateral and axial resolution, respectively (left scale). This depicts the transition from Eqs (5.5) to (5.11) for lateral resolution and the analog transition from Eqs (5.13) to (5.15) for axial resolution. The gray line shows the detection yield as a function of the pinhole diameter (right scale).

second term becomes prominent and the axial resolution of the detection PSF varies almost linearly with the pinhole size. In the case of small pinholes (diameter < 1 AU), the width of the detection PSF is dominated by the first term in Eq. (5.12) and can be approximated by

$$\text{FWHM}_{\text{det;axial, PH} \sim 1\text{AU}} = \frac{0.88\lambda_0}{n - \sqrt{n^2 - \text{NA}^2}} \quad (5.13)$$

The *total* PSF depends on the relative size of the excitation and detection PSFs. When the excitation PSF is significantly larger than the detection PSF, the FWHM of the total PSF will be determined by the detection PSF and, therefore, increases with the pinhole size. When the excitation PSF is smaller than the detection PSF, the total PSF will be given by the excitation PSF. This can be seen in Figure 5.6. The lateral and axial resolution are shown as a function of pinhole size. The prefactors plotted represent the number before $\lambda_0/\text{NA}_{\text{Objective}}$ in Eqs (5.6) and (5.11) for the lateral resolution and before $\lambda_0/(n - \sqrt{n^2 - \text{NA}^2})$ in Eqs (5.12) and (5.13) for the axial resolution. The prefactors saturate for larger pinholes.

Box 5.3 Wavelength Corrections

In the text, we have not discriminated between excitation (λ_{exc}) and emission wavelength (λ_{em}) for the calculations. Because of the Stokes shift, the excitation and emission wavelengths are usually separated by 20–50 nm. To obtain the

(Continued)

Box 5.3 (Continued)

closest possible result, λ_0 has to be replaced by an average wavelength:

$$\lambda_{AV} = \sqrt{2} \frac{\lambda_{em} \lambda_{exc}}{\sqrt{\lambda_{exc}^2 + \lambda_{em}^2}} \quad (5.14)$$

While defining the excitation wavelength λ_{exc} is easy, as modern lasers are monochromic and even diode lasers have a narrow bandwidth of only a few nanometers, the emission wavelength λ_{em} should be weighted by the emission spectrum to obtain the correct average wavelength.

If the size of the pinhole becomes extremely small (diameter ≤ 0.25 AU), not only the *geometric-optical* term in Eq. (5.12) vanishes but also diffraction effects of the pinhole play a significant role. The product with the excitation PSF further decreases the width of the total axial PSF, as shown in Figure 5.6:

$$\text{FWHM}_{\text{tot;axial, PH} \sim 0.25 \text{ AU}} = \frac{0.64 \lambda_0}{n - \sqrt{n^2 - \text{NA}^2}} \quad (5.15)$$

Jonkman and Stelzer [15] and Pawley [16] describe the axial resolution of a confocal microscope with the following formula:

$$r_{\text{axial}} = \frac{F \lambda_0 n}{\text{NA}^2} \quad (5.16)$$

where F is a normalization factor that varies from 1.4 to 2.0 depending on the size of the pinhole and is also referred to as the *focal depth*. As a practical guideline, the confocal pinhole is typically used to control the optical section thickness of the microscope rather than to gain the best possible resolution in the lateral dimension. The axial resolution is at least 3–4 times worse than the resolution in the lateral dimension.

Table 5.1 compares the theoretically achievable resolution in widefield and confocal microscopy for two different objectives – an air and a water objective – assuming an excitation wavelength of 500 nm, a detection wavelength of 520 nm, and the usage of a pinhole size of 1 AU. For high-NA objectives, the increase in axial resolution is larger (about a factor of 1.6) than the improvement in lateral resolution (about a factor of 1.4).

Box 5.4 Increasing the Confocal PSF Size

For single-molecule studies in solution, the photons detected from a single molecule diffusing through the focus of a confocal microscope are collected and analyzed. To allow more photons to be collected, it is often useful to work with a larger focus size, as the amount of time a single molecule spends in the observation volume can be increased by a factor of ~ 10 . This is achieved by not fully filling the back aperture of the objective with the laser beam. By reducing the size of the laser beam, the effective excitation NA of the system is decreased, leading to a larger diffraction-limited volume in both the lateral and

Table 5.1 Exemplary comparisons of the axial and lateral resolution limit for widefield and confocal microscopy for two different objectives by means of the FWHM of the respective PSF.

FWHM	Widefield (nm)	Confocal (nm)
NA = 0.5, $n = 1.00$		
Lateral	530	374
Axial	4896	3348
NA = 1.27, $n = 1.33$		
Lateral	208	147
Axial	759	480

First two rows: $\lambda_{\text{exc}} = 500$ nm, $\lambda_{\text{det}} = 520$ nm, PH = 1 AU, NA = 0.5, and $n = 1$. These values were used for the simulation of Figure 5.7. The lower two rows represent the maximum achievable resolution with high NA water-immersion objectives. Here, the values of the NA and n change to 1.27 and 1.33, respectively.

axial dimensions. In this case, the ratio of axial to radial size will increase from ~ 3 to 4, as discussed previously, to a value between 5 and 8, depending on what fraction of the back aperture of the objective is filled with the laser beam.

5.2.3 Scanning Confocal Imaging

The light passing through the pinhole in confocal microscopy is typically detected either on a point detector or a small number of pixels of a camera. Therefore, to record an image, it is necessary to perform a scan of the sample. It is the scanning, in addition to the pinhole, that differentiates a confocal microscope from other optical instruments. Confocal microscopes can be classified by the technique with which the laser and sample are scanned with respect to each other. The most typical scanning approaches are discussed in the following.

5.2.3.1 Stage Scanning

The simplest and most straightforward approach for scanning a sample is stage scanning. This approach was successfully implemented by Minsky in his first confocal microscope. The optics remains stationary while the sample is scanned, and the intensity of each point is measured before moving the sample to the next position. This technique is still widely used today, especially in the material sciences, and offers several advantages: a confocal microscope with stage scanning is straightforward to build with a minimum of optical elements, is very stable, and can be easily aligned. The scanning can be done very precisely using modern piezo scanners that can move the sample in three dimensions with a resolution on the subnanometer scale. Scanning in the z -direction is important when one wishes to exploit the optical sectioning capability of confocal microscopy to collect 3D information. However, stage scanning also suffers from one drawback: the sample has to be moved. Biological samples are

often sensitive to movement, and the recorded image may be distorted if the specimen shifts during scanning. It is more difficult to interact with the sample, for example, to manipulate the sample with micropipettes unless they are mounted on the scanning stage. The maximum scan speed for piezo scanners is limited, and there is typically a significant relaxation time of several milliseconds or longer for the piezo scanner to move to a new position. This can make the application of piezo scanners difficult for applications where quick and precise control of the sample and laser beam with respect to each other is crucial.

5.2.3.2 Laser Scanning

A second approach to recording confocal images is raster-scanning of the light beam over the sample while leaving the sample stationary. Raster scanning is older than the idea of the confocal microscope [17]. However, it was first in 1987 that White *et al.* successfully combined the techniques of laser scanning and confocal microscopy [10]. The method of laser scanning typically uses a pair of galvanometric mirrors that are controlled by the acquisition software in order to move the beam in x - and y -dimensions. Figure 5.7a shows one possible setup for a laser scanning confocal microscope (LSCM), where two mirrors that scan the beam in perpendicular directions are closely spaced. To avoid clipping of the beam by the objective, a telescope is built into the optical path after the scan mirrors, which images an intermediate position between the two mirrors on the back aperture of the objective. This means that the position of the excitation beam with respect to the objective is relatively stationary while the angle of the beam changes. Hence, the position of the beam on the sample will change with mirror positions, but the position of the light path entering the back aperture of the objective will be stationary. Although the configuration in Figure 5.7a is sufficient for most imaging purposes, it is not ideal and can be improved as shown in Figure 5.7b. Here, a telescope is installed between both mirrors to project the image of the first mirror onto the second mirror. An

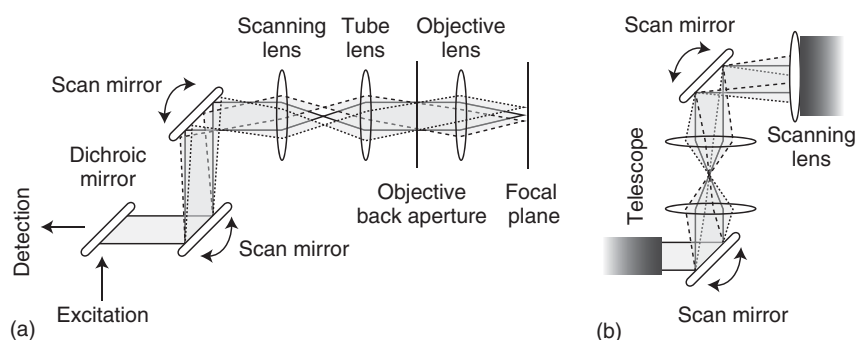


Figure 5.7 Two approaches to laser scanning. (a) A straightforward approach is to position the two mirrors close together. A telescope, usually with the tube lens as one of the elements, is then used to image the plane in between the two mirrors onto the back aperture of the objective. The telescope ensures that the excitation beam is not clipped by the back aperture of the objective during scanning. (b) A second, more elegant approach is to also insert a telescope between the two scanning mirrors. Hence, the first mirror is imaged onto the second, which is then imaged onto the back aperture of the objective.

additional telescope is used to image the second mirror on the back aperture of the objective. When correctly aligned, the excitation beam is stationary at the back aperture of the objective, passes through the objective, and excites a given position of the specimen depending on the angles of the two mirrors. Using galvanometer mirrors, scanning can be performed at almost video rates. When one is willing to give up the flexibility in scan speed, a resonance scanner can be used, which allows higher frame rates to be achieved.

Laser scanning also has its price. One has to live with the fact that the beam is almost always off-axis. Hence, the alignment of the optics is more critical, and excellent optics is needed to minimize off-axis spherical and chromatic aberrations.

5.2.3.3 Spinning Disk Confocal Microscope

Although modern technology has significantly improved the performance of LSCMs, it is still necessary to find a good compromise between the pixel dwell time for good photon statistics and a reasonable scanning speed for every measurement. In general, one is able to obtain acquisition speeds in the range of seconds (depending on the scanner type, the size of the scan region, etc.). Nevertheless, this is often too slow for observing many dynamic biological processes, particularly when one is interested in real-time dynamics. An alternative is the SDCM.

SDCM combines the advantages of confocal microscopy with real-time data acquisition rates known from widefield microscopy. The scan speed is increased by simultaneously scanning multiple pinholes across the sample. The scanning technique used for spinning disk microscopy was developed already in 1884 by the German engineer Nipkow for a machine he called an *electric telescope* [18]. The core element of his invention was a disk (now known as the *Nipkow disk*) with a series of holes arranged in an Archimedean spiral (shown in Figure 5.8). When this disk is placed in front of an image, only sections of the image that are in front of a hole are allowed to pass. The holes are arranged such that each section of an image is scanned for the same amount of time during one revolution of the disk. By spinning the disk, it is possible to translate the image into a series of analog signals which can subsequently be reassembled into an image by passing light through another disk with the same arrangement of holes. This method of mechanical signal transmission was used for the first television broadcasts in the 1920s, but could not compete with the completely electronic method using cathode ray tubes known as *Braun tubes*. Thus, Nipkow disks slid into oblivion for almost 40 years until 1967 when Egger and Petran recognized the relevance of this tool for confocal microscopy [9].

By placing a Nipkow disk with its array of pinholes in a conjugate image plane of the objective, as shown in Figure 5.8a, it is possible to scan every point of the sample successively in a very short time (down to 1 ms) compared to an LSCM. An image of the pinhole structure from a nonrotating Nipkow disk is shown in Figure 5.8b. The excitation beam is split by the disk into an array of beams that create individual focal volumes. To produce the confocal detection and reassemble the distinct fluorescence signals from the different pinholes in the correct order, it is possible to use either conjugated pinholes

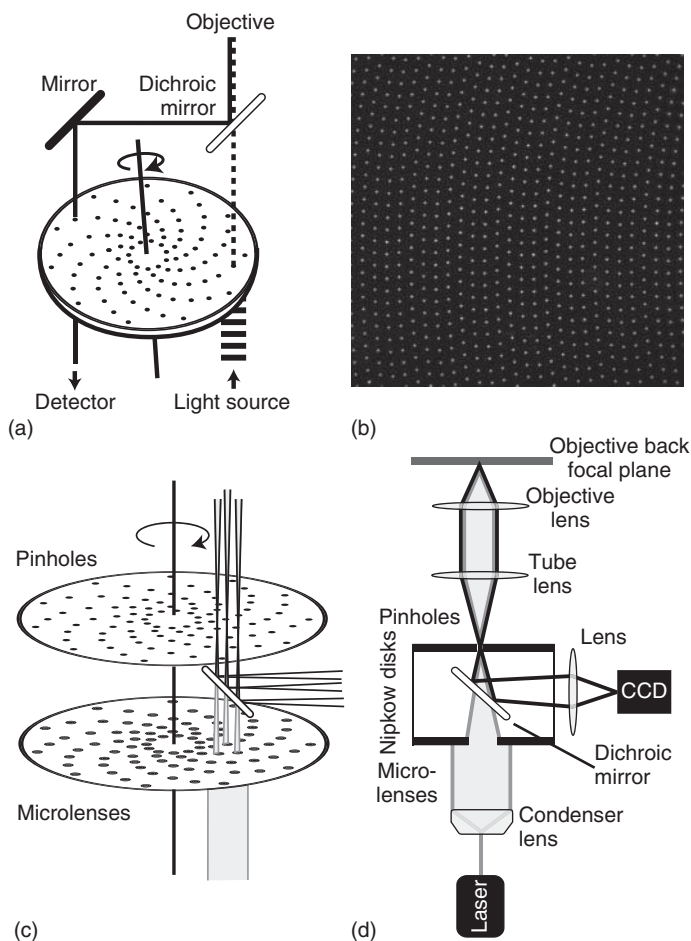


Figure 5.8 Spinning disk confocal microscopy. (a) Schematic of a Nipkow disk and sketch of scanning head of a tandem scanning disk microscope, which uses different regions of the same Nipkow disk for excitation and detection, respectively. (b) Image of the pinhole structure taken from a nonrotating Nipkow disk. (c) Schematic of a SDCM setup with two Nipkow disks, one containing the pinholes and a second one filled with microlenses for increasing the excitation intensity through the pinholes. Gray, excitation light; white with black borders, detection light. (d) Schematic of the excitation (gray) and detection (white with black borders) pathways in an SDCM.

located on diametrically opposed spirals for excitation and detection, as shown in Figure 5.8c (tandem disk scanning microscope), or the same set of pinholes for excitation and detection pathway as shown in the experimental setup in Figure 5.8d (single-sided disk scanning microscope). The latter method is preferred owing to the lower required maintenance efforts. As multiple detection volumes are measured simultaneously, a camera is used for the detection of the confocal image rather than an APD or a PMT. Thus, the microscope can benefit from the high quantum efficiency of CCD cameras. For correct image reproduction, the frame rate of the camera has to be synchronized with the

rotation frequency of the Nipkow disk. Otherwise, the disk rotations will be incomplete, leading to unequal illumination of the image, which appears as a striped pattern on the image. This is particularly important when the collection times are short.

There are several parameters that have to be considered in determining the optical configuration of a Nipkow disk. Because of the design of the Nipkow disk, a considerable amount of the excitation light is blocked. The transmission factor or fill factor T for an SDCM is given by

$$T_{\text{pinhole}} = \left(\frac{D}{S}\right)^2 \quad (5.17)$$

where D is the diameter of the pinhole and S is the distance between the distinct apertures. T is generally much lower for SDCMs compared to LSCMs. In order to provide some rough estimate, about 50% of the excitation light passes through the pinhole of a confocal point-scanning microscope, whereas only about 5% is achievable with a pinhole-based SDCM. The transmission factor can be improved by decreasing the spacing between pinholes or by replacing the pinhole of a confocal microscope with a slit-shaped aperture. For a slit-based confocal microscope

$$T_{\text{slit}} = \left(\frac{D}{S}\right) \quad (5.18)$$

where D is the width of the slit and the transmission is typically $\sim 10\%$. However, the use of slit-shaped pinholes or closely spaced apertures leads to the problem of cross-talk between the pinholes. This means that light coming from out-of-focus regions, which would be blocked by the respective pinhole, is able to pass through the neighboring pinholes and thereby decreases the axial resolution (see below). For this reason, most commercially available systems are based on pinholes with a low fill factor. To compensate for the low throughput of the excitation beam, a microlens system, first presented by the Yokogawa Company, is typically used. In the Yokogawa design, a disk of microlenses is arranged in the same pattern as the pinholes on the Nipkow disk and rotated synchronically, as shown in Figure 5.8c,d. With the microlenses, the fill factor can be increased up to a value of about 40%. However, to reach this value, it is also important to use the optimal pinhole size. On the one hand, a significant amount of excitation light is blocked when a small D or a relatively large S is chosen. On the other hand, when D is too large or S too small, pinhole cross-talk increases. Thus, the spacing S is chosen to find the best balance between minimum pinhole cross-talk, optimum scanning speed, and sample exposure.

While the lateral resolution of the SDCM is similar to that of other confocal imaging methods and the choice of 1 AU is typically a good compromise, the axial resolution is notably influenced by pinhole cross-talk, which can significantly reduce the optical sectioning capacity of the microscope. For very thin samples with a small pinhole (~ 0.25 AU), Eq. (5.15) can be used in good approximation to estimate the optical sectioning capacity of an SDCM using a prefactor of 0.67 for a disk of pinholes and 0.95 for a slit aperture. Otherwise, Eq. (5.12) can be used for the detection PSF, but neither Eq. (5.12) nor Eq. (5.15) takes into account potential pinhole cross-talk. As this effect also depends on nonquantifiable

Table 5.2 Comparison of SDCM with LSCM.

Advantages of the SDCM	Disadvantages of the SDCM
Faster scanning capabilities	Low transmission factors
Can be combined with higher quantum-yield detectors	Lower flexibility (e.g. fixed pinhole size)
Higher biocompatibility as a result of a reduction in excitation energy per unit area	Lower axial resolution

parameters such as the labeling density of the respective sample, it is difficult to give a specific formula for the actual z -resolution. In short, pinhole cross-talk is small when the fluorescence labeling is confined to a thin layer. Otherwise, signal from out-of-focus regions will be able to pass through adjacent pinholes. Of course, it is possible to increase the axial resolution by reducing the pinhole size or increasing the distance between the pinholes, but, as explained above, this goes at cost of signal quality.

In addition to the SDCM, there are multiple ways of generating and scanning multiple points on the sample. One possibility is to use two-photon excitation with a holographic beam splitter to generate multiple excitation beams or by scanning a two-dimensional (2D) array of pinholes rather than a disk in the appropriate conjugate image plane. While in all cases the scanning speed can be improved, this improvement is not possible without making compromises (cf. Table 5.2). Nevertheless, as suggested by the importance Minsky placed on real-time imaging, SDCM and similar approaches have become an extremely valuable tool, as they combine the high contrast of confocal microscopy with the fast data acquisition available from widefield microscopy. By scanning with multiple pinholes simultaneously, the excitation power is more distributed both spatially and temporally over the sample, which can lead to a lower excitation power per unit area and thus higher biocompatibility compared to LSCM.

5.2.4 Confocal Deconvolution

Despite the improvement in image contrast, confocal microscopy images are still diffraction-limited. In order to circumvent this diffraction limit, it is possible to apply super-resolution microscopy methods such as those described in Chapters 8–10. However, it is also possible to improve the resolution of confocal images by performing a deconvolution. The decrease in optical resolution in confocal microscopy is due to the convolution of the actual image with the diffraction-limited PSF of the microscope. Mathematically speaking, the detected signal $S(r)$ at a spatial coordinate r is given by the convolution of the signal $O(r)$ from the original object with the point spread function $\text{PSF}(r)$:

$$S(r) = O(r) \otimes \text{PSF}(r) = \int_{-\infty}^{\infty} O(r') \text{PSF}(r - r') dr' \quad (5.19)$$

When two of the functions are known – as is the case for the observed signal $S(r)$ and the point spread function $\text{PSF}(r)$ – the third function – in this

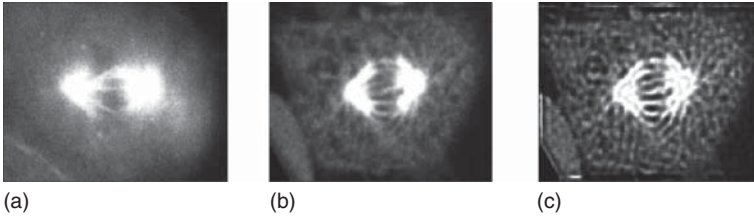


Figure 5.9 Improving resolution by confocal microscopy and confocal deconvolution. (a) A standard widefield image of a tubulin-labeled cell undergoing mitosis. (b) A confocal image of the same cell as shown in (a). The improvement in contrast is clearly visible. (c) The same image as shown in (b) deconvoluted using the Richardson–Lucy algorithm.

case the actual spatial distribution $O(r)$ of the object – can be determined. In practice, noise or limited information regarding one or both of the known functions can make deconvolution difficult to impossible. Thus, $O(r)$ cannot be straightforwardly obtained by using Eq. (5.19), but more complex deconvolution algorithms have to be applied.

Figure 5.9 shows the image of a tubulin-labeled cell undergoing mitosis. Compared with the widefield image (Figure 5.9a), the confocal image (Figure 5.9b) already shows a significant improvement in contrast. An additional improvement is seen in the deconvoluted image (Figure 5.9c) where the complete structure of the spindle apparatus is resolved.

One prominent deconvolution approach is the Richardson–Lucy algorithm, which was used in Figure 5.9 [19]. The signal detected in an image depends on the original distribution of signal from the object and the probability that emitted signal through the PSF of the system ends up in the respective pixel. When u_{kl} represents the intensity originating from pixel k, l and $\text{PSF}_{ij:kl}$ is the probability of light that originated from location k, l , being detected at location i, j , the detected signal in pixel i, j is given by

$$d_{ij} = \sum_{k,l} \text{PSF}_{ij:kl} u_{kl} \quad (5.20)$$

If u_{kl} is Poisson-distributed, which is the case when the dominant noise source is the photon noise, one can iteratively calculate the most probable value for $u_{kl}^{(t+1)}$ at iteration step $t + 1$ when all other parameters from Eq. (5.20) are known:

$$u_{kl}^{(t+1)} = u_{kl}^t \sum_{i,j} \text{PSF}_{ij:kl} \frac{d_{ij}}{\sum_{kl} \text{PSF}_{ij:kl} u_{kl}^t} \quad (5.21)$$

It has been shown that, when these iterations converge, the result will be the maximum likelihood for u_{kl} .

For a more accurate deconvolution, detailed knowledge of the PSF is required. Close inspection of the lower left corner of Figure 5.9c shows that the PSF might have changed in this region owing to aberrations in the objective, and the deconvolution does not yield the correct value for u_{kl} in this part of the image. When the PSF is not known, the quality of the image can still be enhanced by using *blind deconvolution*, where the PSF is estimated in an iterative process.

5.3 Applications of Confocal Microscopy

For the biological sciences, the main application of confocal microscopy is imaging. It has become routine to record multicolor 3D images using a confocal microscope. An example of a 3D confocal image recorded using an SDCM is shown in Figure 5.10 and also given in the online material. Here, the plasma membrane of an HMEC-1 cell has been labeled in red and the mitochondria have been labeled in green. The structure of the complex 3D network of the mitochondria is clearly visible throughout the cell. Also early endosomes, which are labeled by internalization of the membrane marker, can be distinguished from the plasma membrane via the position and morphology of the measured signal.

Although imaging is the most common application of confocal microscopy, there are many important applications in the biochemical and biophysical sciences that go beyond imaging. In the following sections, we discuss a number of fluorescence fluctuation spectroscopy techniques that utilize confocal microscopy.

5.3.1 Nonscanning Applications

5.3.1.1 Fluorescence Correlation Spectroscopy

FCS is a versatile technique to extract information out of fluctuations in fluorescence intensity. Several detailed papers and reviews can be found in the literature (e.g., [20–22]). FCS was first published in the beginning of the 1970s by Magde, Elson, and Webb [23, 24]. The method analyzes the temporal fluctuations of the fluorescence intensity using a correlation analysis to gain information regarding the processes responsible for the fluctuations. Along with the development of ultrasensitive detectors and stable laser light sources, it was the use of a small confocal detection volume (~ 1 fl) that made it possible

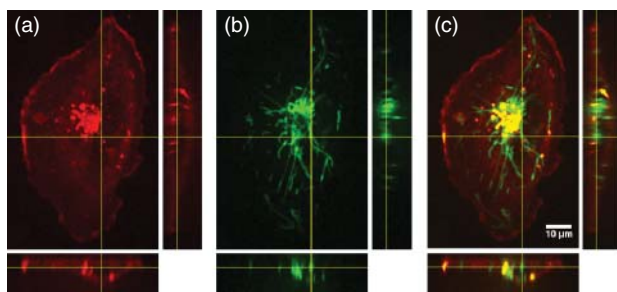


Figure 5.10 Three-dimensional (3D) confocal imaging. Images of a HMEC-1 cell are shown, where different organelles have been labeled with different colors. Slices of the three-dimensional image in the x - y , x - z , and y - z planes are shown for (a) membrane labeling using CellMask™ (deep red, Life Technologies) (red) and (b) the mitochondria labeled with MitoTracker® (Green FM, Life Technologies) (green). (c) A merged image is shown where early endosomes, indicated by the internalized membrane marker, are shown in yellow. The various structures of the plasma membrane, mitochondria network, and endosomes are clearly distinguishable via the improved 3D resolution of confocal microscopy. A 3D representation of these images can be found in the online material.

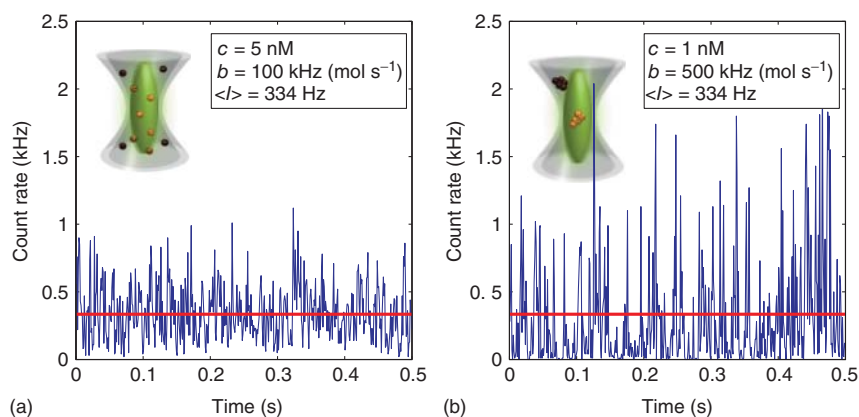


Figure 5.11 Fluorescence intensity fluctuations at low concentration. (a) Simulation of a sample of molecules with a concentration, c , of 5 nM and a molecular brightness, b , at the center of the PSF of 100 kHz per molecule. (b) Simulation of a sample at 1 nM concentration with a molecular brightness of 500 kHz per particle at the center of the PSF. The average intensity $\langle I \rangle$ is equal in both cases.

to detect signals down to a single fluorophore [25]. This sensitivity has made FCS easily applicable to a broad range of applications. Figure 5.11 shows the intensity versus time trace for two species with different concentrations and molecular brightnesses freely diffusing in solution. The two samples were chosen to have the same average fluorescence intensity (solid line). However, the fluctuations in the fluorescence intensity are very different for the two samples, with the fluctuations from the brighter species at lower concentration being larger. The variations in fluorescence intensity arise from thermodynamic fluctuations in the number of particles within the confocal detection volume due to Brownian motion. By analyzing the temporal fluctuations in fluorescence intensity, information can be extracted regarding the average number of particles in the volume as well as the average time it takes for them to travel through the confocal volume. When the shape and size of the confocal volume is known, it is possible to convert the average number of molecules and the time they spend in the confocal volume into an average concentration and a translational diffusion coefficient. FCS is not limited to diffusion; any process that leads to fluctuations in fluorescence intensity can be analyzed with FCS. Hence, it is possible to measure, for example, singlet–triplet state dynamics and the rate of chemical reactions (when the reaction leads to a change in molecular brightness) even though the measurements are performed in equilibrium.

To extract the information buried in the fluctuations of the fluorescence signal, a correlation analysis is used. The photons detected from the same molecule will lead to a correlation signal, whereas randomly detected photons from noncorrelated processes do not correlate. The correlation process is highly sensitive and can be used to determine the timescale over which two signals remain similar, or, in the case of the autocorrelation analysis, how long the fluctuations of a single signal persist on average. Consider the fluctuations due to molecules diffusing in and out of a confocal focal volume. The fluorescence signal will fluctuate as

molecules enter and leave the focus. The average timescale of the fluctuation depends on the time a molecule needs to cross the confocal spot, referred to as the *diffusion time* τ_D . τ_D depends on the size of confocal volume and on the diffusion coefficient D . On timescales shorter than or equal to τ_D , the position of molecules within the volume does not change significantly and the detected signal remains similar. On longer timescales, molecules can enter or leave the confocal volume, the fluorescence signal changes, and the correlation drops. Hence, for times longer than τ_D , the correlation function decays.

The derivation of the autocorrelation for FCS can be found, for example, in Elson and Magde [23]. For a measurement with freely diffusing molecules in three dimensions, the intensity of the fluorescence signal F at a certain time t is given as

$$F(t) = \epsilon \int dr \overline{W(r)} C(r, t) \quad (5.22)$$

where ϵ is the molecular brightness, $C(r, t)$ is the number density of molecules at a certain position r at time t , and $\overline{W(r)} = W(r)/W(0)$ is the normalized PSF, with $W(0)$ being the laser intensity at the center of the PSF. The molecular brightness ϵ is defined as the fluorescence intensity of a single fluorophore at the center of the PSF and is given by

$$\epsilon = \kappa \sigma_{\text{Abs}} \phi W(0) \quad (5.23)$$

where κ is the total detection efficiency of the microscope, σ_{Abs} is the absorption cross section of the fluorophore at the wavelength of the laser, and ϕ is the fluorescence quantum yield of the fluorophore. The autocorrelation function (ACF) is given by

$$\begin{aligned} G(\tau) &= \frac{\langle \delta F(t) \delta F(t + \tau) \rangle}{\langle F(t) \rangle^2} = \frac{\langle F(t) F(t + \tau) \rangle - \langle F(t) \rangle^2}{\langle F(t) \rangle^2} \\ &= \frac{\langle F(t) F(t + \tau) \rangle}{\langle F(t) \rangle^2} - 1 \quad \text{with } \delta F(t) = F(t) - \langle F(t) \rangle \end{aligned} \quad (5.24)$$

where $\langle \rangle$ represents the time-averaged value. A graphical interpretation of the ACF is shown in Figure 5.12. During the correlation analysis, the signal is shifted by a time interval τ , multiplied with the original curve, and integrated over the fluorescence time trace. In the end, the correlation analysis is normalized by the square of the average fluorescence intensity and 1 is subtracted.

The PSF of a confocal microscope can be approximated as a 3D Gaussian:

$$W(r) = W(0) \exp \left[- \left(\frac{(x^2 + y^2)}{2\omega_r^2} \right) - \left(\frac{z^2}{2\omega_z^2} \right) \right] \quad (5.25)$$

where ω_r and ω_z are the dimensions of the PSF from the center to the position where the intensity has decreased by a factor $1/e^2$ in the lateral and axial directions, respectively. Substituting Eqs (5.22) and (5.25) into Eq. (5.24), we obtain an analytical form for the ACF of a freely diffusing particle:

$$G_D(N, D, \tau) = \frac{\gamma_{\text{FCS}}}{N} \left(\frac{1}{1 + (\tau/\tau_D)} \right) \left[\frac{1}{1 + (\omega_r/\omega_z)^2 \cdot (\tau/\tau_D)} \right]^{\frac{1}{2}} \quad (5.26)$$

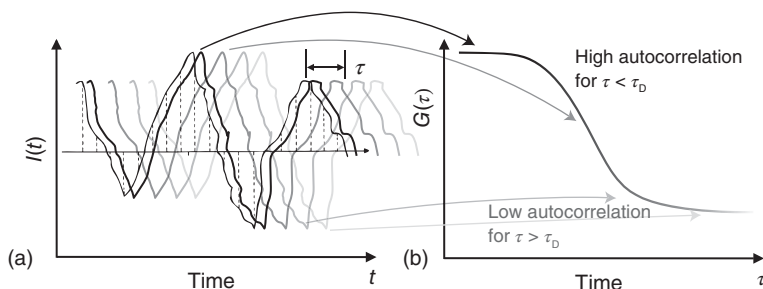


Figure 5.12 Determination of the autocorrelation function. (a) A schematic of a fluorescence signal (black curve) fluctuating about a mean value (black horizontal line) and (b) the resulting autocorrelation function. The trace is duplicated and shifted by different time delays τ (different gray values). The shifted curve is multiplied with the original curve and integrated to determine the residual self-similarity of the signal. The similarity decays from black to light gray, which can be seen by the drop in the correlation amplitude.

where $\langle N \rangle$ is the average number of particles in the confocal volume, γ_{FCS} is a geometrical factor that depends on the shape of the volume ($\gamma_{\text{FCS}} = 2^{-3/2}$ for a 3D Gaussian PSF), and $\tau_D = \omega_r^2/4D$ is the diffusion time.

One can also define the ACF as

$$g(\tau) = \frac{\langle F(t)F(t+\tau) \rangle}{\langle F(t) \rangle^2} = G(\tau) + 1 \quad (5.27)$$

The expression for the ACF shown in Eq. (5.27) is proportional to the probability of detecting a photon at a delay time τ when a photon was detected at the time $t=0$. For timescales much smaller than the diffusion time τ_D , the molecule still remains in the confocal volume, and so the probability to detect a second photon is high. On longer timescales, this probability decreases owing to the possibility that the particles leave the confocal focal volume via Brownian motion and no further photon is detected. A correlation analysis is powerful, as it is capable of detecting any type of fluctuation in fluorescence intensity that is not stochastic. Examples of processes that can be detected using FCS are shown in Figure 5.13.

The full correlation function here consists not only of the term arising from diffusion but also terms due to photon anti-bunching, rotational motion, and blinking of the fluorophore when it enters and escapes the triplet state. Fortunately, these influences take place on different timescales and are distinguishable. While FCS analyzes the temporal behavior of the fluorescence intensity, there are other methods available that make use of the amplitudes of the fluctuations to gather information regarding the average number of molecules and their molecular brightness such as the photon counting histogram (PCH) analysis, fluorescence intensity distribution analysis (FIDA), and cumulant analysis. For an excellent introduction to the different brightness analysis methods, we refer the reader to Macdonald *et al.* [26].

The amplitude of the ACF is inversely proportional to the number of particles in the confocal volume. For a single species, the amplitude of the ACF is independent of the molecular brightness, whereas the signal-to-noise ratio

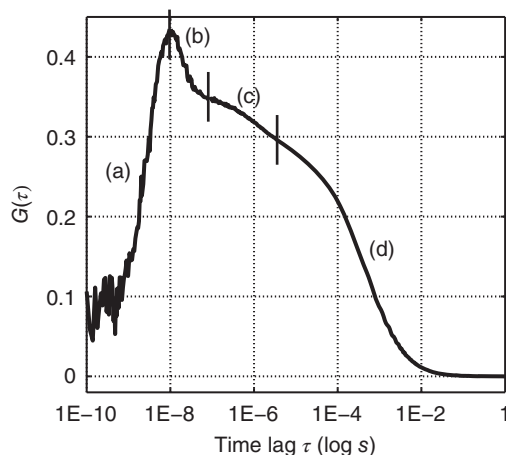


Figure 5.13 The measured ACF of green fluorescent protein (GFP) in aqueous solution. A number of processes can be detected by FCS as highlighted in the ACF: (a) anti-bunching, which emerges because the fluorophore has to be re-excited before it can emit a second photon (to detect anti-bunching, two detectors are necessary to avoid the dead time of detectors and data collection card), (b) rotational diffusion, (c) intramolecular reactions such as transitions between the singlet to the triplet states, and (d) translational diffusion.

depends on the molecular brightness but is independent of sample concentration, at least in the range where FCS is most sensitive (from ~ 100 pM to ~ 100 nM).

5.3.1.2 Fluorescence Cross-Correlation Spectroscopy

It is also possible to correlate two signals with each other, a method known as *cross-correlation*. Typically, two detection channels sensitive to different wavelengths are used, and the fluorescence signals from the two channels are cross-correlated. This method of dual-color fluorescence cross-correlation spectroscopy (FCCS) is well suited for investigating the interaction of molecules [27]. Figure 5.14 shows the autocorrelation and cross-correlation of double-stranded DNA that is labeled on one strand with Atto532 and on the second strand with Atto647. A strong correlation is expected, as the DNA is double-labeled with high efficiency and a fluctuation in green channel due to a DNA molecule entering the confocal volume will be correlated with an increase in signal in the red channel.

The number of double-labeled molecules detectable in both channels, N_{12} , can be extracted from the amplitude of the cross-correlation function (CCF). Assuming two overlapping 3D Gaussian confocal volumes and that the system is cross-talk-free, the CCF is given by

$$G_D(N, D, \tau) = \frac{\gamma_{\text{FCS}} \langle N_{12} \rangle}{\langle N_1 + N_{12} \rangle \langle N_2 + N_{12} \rangle} \left(\frac{1}{1 + (\tau/\tau_D)} \right) \left(\frac{1}{1 + (\omega_r/\omega_z)^2 \cdot (\tau/\tau_D)} \right) \quad (5.28)$$

where γ_{FCS} is a geometrical factor equal to $2^{-3/2}$ when the PSF is approximated with a 3D Gaussian, N_i is the number of molecules of type i (where i can be single-labeled molecules visible in channel 1 or 2, or double-labeled molecules), and $\tau_D = \omega_r^2/4D_{12}$ is the diffusion time of the double-labeled molecules where D_{12} is the diffusion coefficient for the double-labeled species. Although the CCF is often used as a digital answer to a problem – whether two molecules interact – the amplitude of the CCF itself and its relative height with respect to the autocorrelation function contain information regarding the percentage of complexes carrying both fluorophores. A detailed description of how to perform

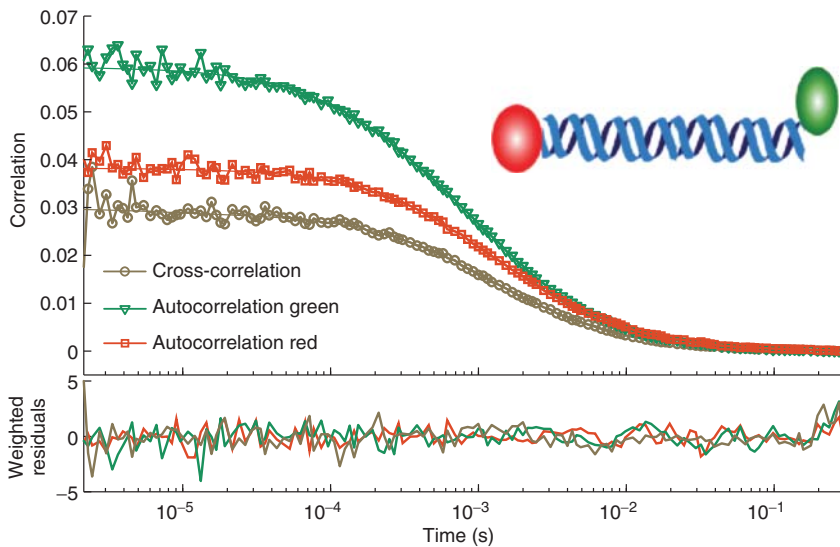


Figure 5.14 Cross-correlation of double-labeled DNA. Double-stranded 60 bp DNA was labeled at the ends with Atto532 and Atto647. The autocorrelation functions for Atto532 (green), Atto647 (red), and corresponding cross-correlation function (gold) are shown. The fits are shown as solid lines of the respective color, and the weighted residuals are plotted in the lower panel.

quantitative analysis of FCCS data, in particular with fluorescent proteins, is given in Foo *et al.* [28].

5.3.1.3 Pulsed Interleaved Excitation

The sensitivity of FCCS can be further enhanced with the use of pulsed interleaved excitation (PIE) [29]. PIE is based upon alternating laser excitation (ALEX) [30], developed in the laboratory of Shimon Weiss, with the modifications that subnanosecond pulsed lasers are used for excitation and they are alternated (or interleaved) on the nanosecond timescale. To achieve this, the excitation lasers are synchronized and delayed with respect to each other by 12–20 ns (4–5 times the fluorescence lifetime of the dyes used). For detection, photons can be recorded using a counting board that is synchronized to the excitation lasers. It is then possible to assign every detected photon to its excitation source (Figure 5.15a). A more elegant possibility for data collection is the use of TCSPC detection, which has the additional advantage that lifetime histograms of the fluorophores can be generated and analyzed. With the lifetime information, the presence of quenching, for example, due to Förster resonance energy transfer (FRET, Chapter 13), can be determined.

Figure 5.15b shows the ACFs and CCFs for two noninteracting fluorophores in solution. As correlation spectroscopy is very sensitive to correlated events, the cross-talk signal of the Atto532 fluorophore into the Atto665 channel gives rise to a residual cross-correlation amplitude in the CCF. Spectral cross-talk arises from the tail of the fluorescence emission spectrum of the green fluorophore being detected in the red channel. Spectral cross-talk cannot be totally suppressed

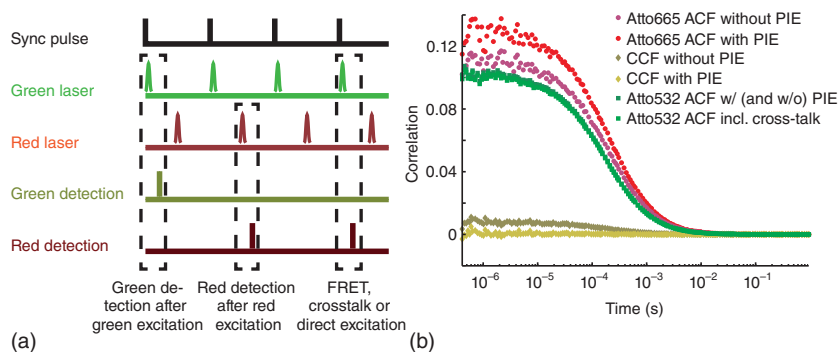


Figure 5.15 Pulsed interleaved excitation (PIE). (a) A schematic showing the principle of PIE. (b) The ACF and CCF for Atto532 and Atto665 freely diffusing in solution determined with and without PIE. The influence of cross-talk and direct excitation on the red ACF and CCF can be observed, which is completely removed when using PIE.

in the red channel by simply using the appropriate emission filter without significantly decreasing the sensitivity of the system to the red fluorophore. Cross-talk affects not only the amplitude of the CCF but also the amplitude of the red ACF as the green fluorophore acts as a second species in the red detection channel. Spectral cross-talk can be totally avoided when using PIE by cross-correlating the photons detected in the green channel after green excitation with photons detected in the red channel after red excitation (light gold data, Figure 5.15b). With the appropriate choice of an emission filter in the green channel, no fluorescence from the red fluorophore will be present in the green channel. Furthermore, with selection of the correct wavelength for red excitation, it is possible to avoid excitation of the green fluorophore. Hence, the PIE CCF is cross-talk-free. In addition, the ACF determined from photons detected in the red channel after red excitation has no spectral cross-talk. Removal of spectral cross-talk results in a quantitatively correct amplitude for the red ACF, as demonstrated by the increase in the amplitude of the red ACF when using PIE (red data, Figure 5.15b). The amplitude of the green ACF is not affected by PIE (light green data, Figure 5.15b). Reassignment of the cross-talk photons to the correct detection channel will increase the detected molecular brightness and can be done when the direct excitation of the red dye (here: Atto665) with the green laser (530 nm) is negligible. An increase in molecular brightness will lead to an improvement of the signal-to-noise ratio of the ACF but will not alter the shape or amplitude of the function when only a single diffusing species is present.

This improvement in FCCS is very important for interaction studies on biological samples, as PIE makes it possible to distinguish between a weak interaction of relevant biomolecules and no interaction at all. As PIE records the detection channel and excitation source for each photon, different channels can be defined *ex facto* and “misplaced” photons can be reassigned to the correct channel. For example, cross-correlating all the photons detected after green excitation with photons detected after red excitation yields CCFs that can be evaluated quantitatively even in the presence of FRET [29].

5.3.1.4 Burst Analysis with Multiparameter Fluorescence Detection

With the small detection volume of a confocal microscope, it is possible to detect single molecules in a dilute sample [31, 32]. When a single fluorescent molecule diffuses through the focus of the microscope, a burst of photons is detected. All of the photons collected from a burst due to a single particle are accumulated and analyzed. To maximize the information that can be extracted from each photon, multiparameter fluorescence detection (MFD) is used (shown schematically in Figure 5.16) [33]. In MFD, the fluorescence emission signal is first split with a polarizing beamsplitter into parallel and perpendicular polarizations, and then both polarization channels are split with a dichroic beamsplitter to separate the photons spectrally.

From the MFD data, it is possible to determine the fluorescence lifetime τ and anisotropy r for the different channels (Figure 5.16b), the molecular brightness η for each species, the fluorescence intensity of each channel, and the arrival time of each photon with respect to the start of the measurement (with 100 ns resolution or better). PIE can be combined with MFD, as shown in Figure 5.17, to add stoichiometry information to the measurement [34].

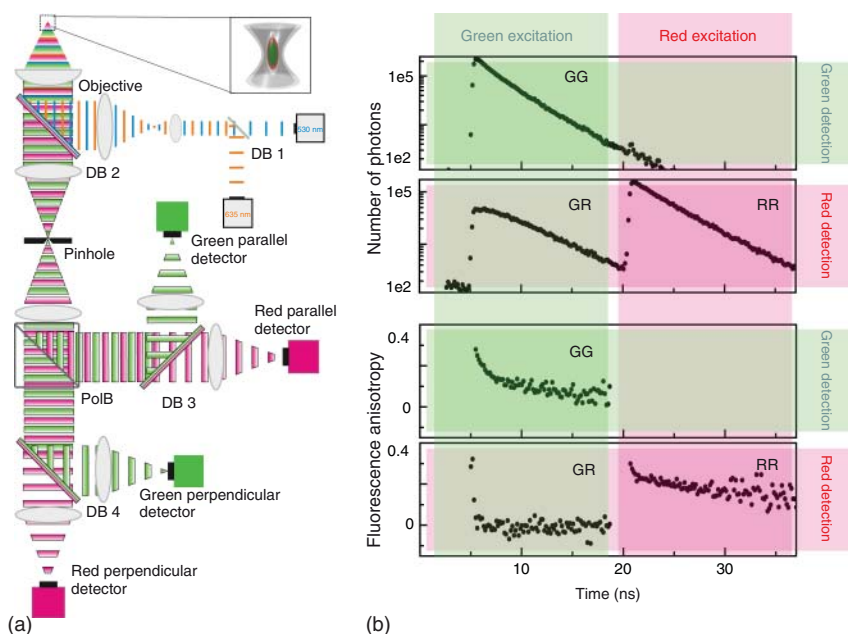


Figure 5.16 Multiparameter fluorescence detection with pulsed interleaved excitation. (a) Schematic drawing of an multiparameter fluorescence detection-pulsed interleaved excitation (MFD-PIE) setup and (b) experimental data of double-labeled DnaK, a bacterial heat-shock protein 70, recorded with MFD-PIE. MFD-PIE allows segregation of photons based on their spectral range, polarization, and the excitation source. The excitation source is assigned according to the arrival time of the detected photon with respect to the synchronization pulse as in PIE. From the MFD-PIE measurements, the stoichiometry, the fluorescence lifetimes of the various channels (upper panel), or the time-resolved anisotropy (lower panel) of the various channels can be determined.

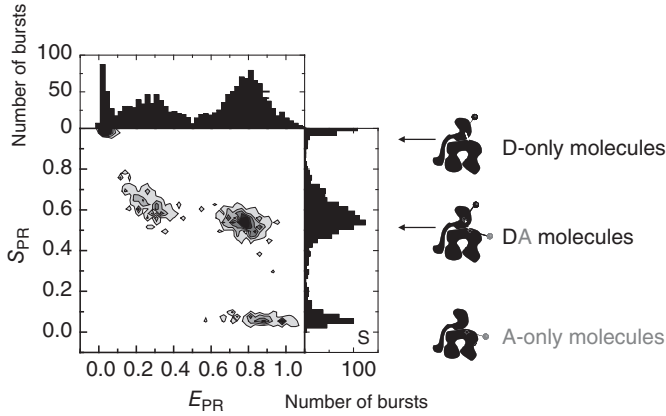


Figure 5.17 FRET efficiency versus stoichiometry plot of double-labeled DnaK molecules. From the stoichiometry values, the donor- and acceptor-only species can be separated from the double-labeled molecules or complexes. Hence, single-pair FRET histograms can be determined that are not contaminated with donor-only molecules.

With dual-color detection, MFD is well suited for performing single-pair Förster resonance energy transfer (spFRET) experiments. When two fluorophores attached to a single molecule or complex are within a distance of $\sim 100 \text{ \AA}$, they will undergo FRET. By measuring the relative intensity of the two channels, the FRET efficiency and thereby the distance between the two fluorophores can be determined. Hence, it is possible to determine structural features and measure dynamics of proteins and other biologically relevant molecules *in vivo* with a resolution down to a few ångströms. In spFRET measurements using MFD, the FRET efficiency for every burst is typically determined from the ratio of the number of transferred photons (I_{FRET}) over the total number of photons in a burst ($I_{\text{FRET}} + I_{\text{Donor}}$):

$$E = \frac{I_{\text{FRET}}}{I_{\text{FRET}} + \gamma I_{\text{Donor}}} \quad (5.29)$$

where γ accounts for the different detection efficiencies of the donor (D) and the acceptor (A) channels, which can either be determined in a different set of experiments or calculated from the respective quantum yields ϕ of the fluorophores and the efficiencies η of the different detection pathways:

$$\gamma = \frac{\eta_A \phi_A}{\eta_D \phi_D} \quad (5.30)$$

The FRET values calculated for the individual molecules are typically plotted in a 1D histogram. When PIE is used, the stoichiometry for every burst can also be determined. The stoichiometry describes the ratio of photons collected after green excitation to the total photons detected:

$$S = \frac{I_{\text{FRET}} + I_{\text{Donor}}}{I_{\text{FRET}} + I_{\text{Donor}} + I_{\text{Acceptor}}} \quad (5.31)$$

where I_{Acceptor} is the number of photons collected in the acceptor channel after red excitation. A 2D histogram of FRET efficiency versus stoichiometry is shown in Figure 5.17 for the bacterial heat-shock protein 70 DnaK. With the help of the stoichiometry value (Eq. (5.31)), it is easy to distinguish proteins labeled with only a single donor or acceptor fluorophore from double-labeled molecules. From the FRET efficiency versus stoichiometry histogram, bursts from double-labeled molecules can be selected and further analyses performed with the data available from MFD. The details that can be extracted from a burst analysis experiment regarding dynamics, subpopulations, distances and so on are impressive. The main limitations in burst analysis experiments are the number of collected photons and the signal-to-noise ratio of the experiment. Hence, the advantages of confocal microscopy have played an important role in the advancement of solution-based single-molecule methods.

5.3.2 Scanning Applications beyond Imaging

There are a number of other methods that analyze the information available in the fluctuations of fluorescent signals. Many of these methods can be performed on image data collected using a confocal microscope. We highlight two of these methods here: the number and brightness (N&B) analysis and raster image correlation spectroscopy (RICS).

5.3.2.1 Number and Brightness Analysis

The effect of particle number and molecular brightness on the average intensity and variance is illustrated in Figure 5.11. Experiments were simulated for two species, A and B, where the molecular brightness of species A is 5 times lower than that of species B, but A is present at 5 times higher concentration. The mean intensity $\langle I \rangle$ is the same for both solutions, but the fluctuations in solution B (Figure 5.11b) – and therefore the variance σ^2 – are significantly larger than in solution A (Figure 5.11a). N&B analysis [35] is the most direct approach for analyzing the fluctuations in an intensity trace or series of fluorescence images. Two assumptions are made for an N&B analysis: only one species with a particular brightness is present within the detection volume, and the detected mean fluorescence intensity $\langle I \rangle$ is directly proportional to the number of molecules n in the detection volume and the apparent brightness b of the fluorescent species:

$$\langle I \rangle = nb \quad (5.32)$$

where b has units of photons per molecule per unit time. The variance of the fluorescence signal will depend upon the fluctuations in the number of fluorescent molecules in the detection volume and the fluctuations due to shot noise of the detected signal. The variance in the fluorescence signal arising from fluctuations in the number of particles within the detection volume due to diffusion, $\sigma_{\text{Particles}}^2$, is proportional to the square of the molecular brightness. The fluctuations in particle number follow a Poissonian distribution, which has the property that the variance of the distribution is equal to the mean value. Hence, the variance in the number of particles in the detection volume is equal to the

average number of molecules:

$$\sigma_{\text{Particles}}^2 = nb^2 = \langle I \rangle b \quad (5.33)$$

Shot noise comes from the fact that fluorescence emission does not occur steadily, but also follows a Poissonian probability distribution:

$$\text{Poi}(k, \lambda) = \frac{\lambda^k e^{-\lambda}}{k!} \quad (5.34)$$

where k is the number of occurrences, and λ is the average number of occurrences (e.g., emitted photons). Hence, the variance from the shot noise is given by the average intensity, $\sigma_{\text{Shot Noise}}^2 = \langle I \rangle$. The total variance in the signal is the sum of the two processes:

$$\sigma^2 = \sigma_{\text{Particles}}^2 + \sigma_{\text{Shot Noise}}^2 = b\langle I \rangle + \langle I \rangle = (b + 1)\langle I \rangle \quad (5.35)$$

Including the shot-noise corrections into Eqs (5.32) and (5.33) yields

$$b = \frac{\sigma^2 - \langle I \rangle}{\langle I \rangle} \quad (5.36)$$

$$n = \frac{\langle I \rangle^2}{\sigma^2 - \langle I \rangle} \quad (5.37)$$

In order to obtain a more meaningful physical property than the number of photons emitted in an arbitrary time interval, the *molecular brightness* ϵ is introduced [36]. Molecular brightness is defined as the number of detected photons per second per molecule when the fluorophore is at the center of the PSF. There is a linear interrelation between the apparent brightness b and the molecular brightness ϵ via the binning time T_{bin} of the fluorescence trace:

$$\epsilon = \frac{b}{T_{\text{bin}}} \quad (5.38)$$

One should keep in mind that the molecular brightness for the same fluorophore may be different when measured with different setups, as it depends on the number of laser photons per second $W(0)$ in the confocal spot and the detection efficiency κ of the entire system (Eq. (5.23)).

The method of N&B provides a straightforward approach to analyze the fluctuations in a given intensity trace or individual pixels from a movie. As it assumes a single species and makes no assumptions regarding the shape of the PSF, it is not as accurate as other brightness-based approaches such as the PCH analysis or FIDA. However, it is quick and easy to calculate and often provides a sufficient amount of information. An example of the N&B analysis is shown in Figure 5.18 [37]. Figure 5.18a shows the fluorescence intensity of DNA methyltransferase 1 in a buffer as a function of time. The overall fluorescence intensity decays as a function of time. From the N&B analysis (Figure 5.18b), we observe that the number of particles decreases with time whereas the molecular brightness remains constant. This suggests that the concentration of DNA methyltransferase 1 is decreasing due to adsorption of the protein to the surface of the sample holder. In Figure 5.18c, the fluorescence intensity of a sample of Atto532 in solution is shown as the laser power is increased in a stepwise

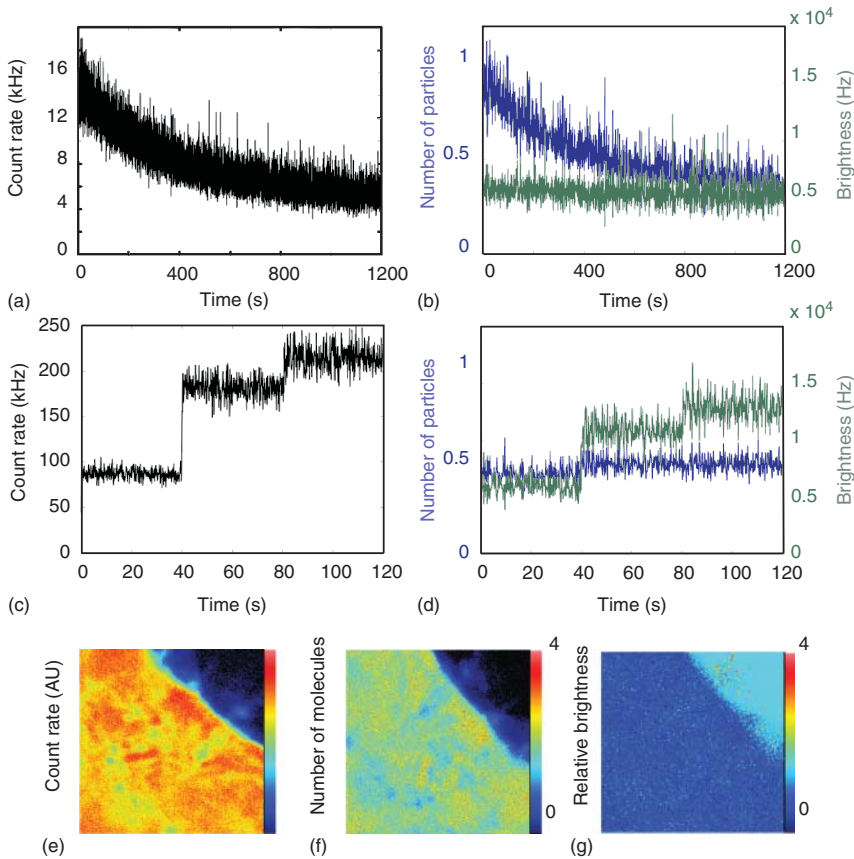


Figure 5.18 Fluorescence intensity traces (black) and N&B analysis (number blue, brightness green) for two different measurements. (a) Measurements of DNA methyltransferase 1 (Dnmt1) in solution. The fluorescence intensity is shown as a function of time. (b) An N&B analysis was performed with a sliding window on the intensity trace shown in (a). The number (blue) and brightness (green) of the molecules are plotted as a function of time. As more and more molecules adsorb to the sample chamber surface, the number of molecules in the solution decreases while the brightness remains constant. (c) The fluorescent intensity of Atto532 in solution. During the measurement, the laser power was increased stepwise. (d) The N&B analysis of the intensity trace shown in (c) using a sliding window. The N&B analysis shows a stepwise increase in the brightness (green) correlating to the changes in laser power, whereas the number of molecules (blue) remains constant. (e) Fluorescence measurements of cytosolic GFP in HeLa cells. An image from the movie is shown. Regions of intermediate and high count rates are visible. (f) The number of molecules and (g) the brightness determined using the N&B analysis for each pixel of the image are shown. (Courtesy of Dr Höller.)

manner during the measurement. As the laser power is increased, the molecular brightness also increases (Eq. (5.22)). This is reflected in the N&B analysis, where the increase in brightness follows the laser power while the number of molecules remains the same (Figure 5.18d).

The strength of N&B analysis is that it can be performed on movies. Figure 5.18e shows the average fluorescence detected from a HeLa cell

expressing the green fluorescent protein (GFP). Variations in the fluorescence intensity are observed. By performing an N&B analysis on each pixel of the image (Figure 5.18f,g), it is clear that the concentration of protein varies within the cytosol whereas the molecular brightness remains the same. While this is a trivial result for GFP alone, it demonstrates the capabilities of the method. When GFP is fused to other proteins, N&B analysis can provide insights into the oligomerization state and stoichiometry of the protein or complex.

5.3.2.2 Raster Image Correlation Spectroscopy

RICS [38] combines LSCM with correlation spectroscopy. One difficulty with point FCS measurements in live cells is photobleaching due to the slow diffusion of biomolecules in the crowded environment of the cell. Photobleaching can be reduced in slowly diffusing media by scanning the laser beam. One possibility is to scan in a circle as in scanning FCS or, alternatively, to raster-scan the sample as is done for imaging and for RICS. In a raster-scanned image (Figure 5.19a), there is a relationship between the spatial separation of pixels in the image and the time delay between when the pixels were measured. As in FCS, the fluctuations are analyzed, but, in RICS, the temporal information is encoded in the spatial information within the image and analyzed using image correlation spectroscopy. As the excitation and detection beams are scanned relative to the sample, it is possible to gather more statistics while minimizing the exposure of each position within the sample to the laser light.

The 2D correlation pattern offers information about the diffusion process along the respective axes, which are scanned on different timescales. The two neighboring pixels in a line (x -axis) are measured consecutively with a time delay given by the pixel clock, whereas two neighboring pixels in adjacent lines (y -axis)

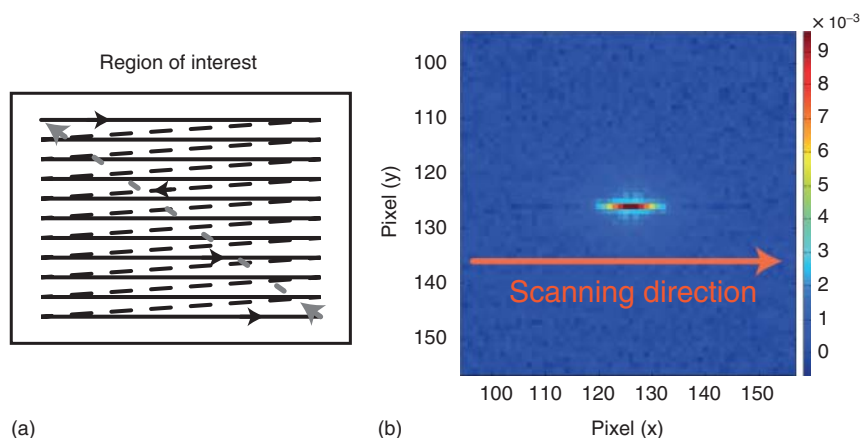


Figure 5.19 Raster image correlation spectroscopy (RICS). (a) The principle of raster-scan imaging with a laser scanning confocal microscope. A line is scanned linearly in time after which the beam is directed to the beginning of the next line and the following line scanned linearly in time. (b) RICS correlation function from series of 50 images (total length 50 μm) of labeled DNA diffusing in solution with a recording time of 500 ms per frame.

are separated by the time it takes to scan a line. In the case of free Brownian diffusion, the RICS ACF assuming one-photon excitation and a 3D Gaussian PSF (Eq. (5.25)) is given by

$$G(\xi, \psi) = \frac{2^{-\frac{3}{2}}}{N} \left(1 + \frac{4D(\tau_x \xi + \tau_y \psi)}{\omega_r^2} \right)^{-1} \left(1 + \frac{4D(\tau_x \xi + \tau_y \psi)}{\omega_z^2} \right)^{-\frac{1}{2}} \times \exp \left\{ \frac{\left[\left(\frac{s\xi}{\omega_r} \right)^2 + \left(\frac{s\psi}{\omega_r} \right)^2 \right]}{\left[1 + \frac{4D(\tau_x \xi + \tau_y \psi)}{\omega_r^2} \right]} \right\} \quad (5.39)$$

where $\langle N \rangle$ is the average number of fluorescent molecules in the PSF, D is the diffusion coefficient of the molecules, τ_x and τ_y are the pixel sampling times in the x - and y -axes, respectively, ω_x and ω_z are the lateral and axial dimensions of the confocal volume, ξ and ψ are the x and y spatial lags in pixels, respectively,

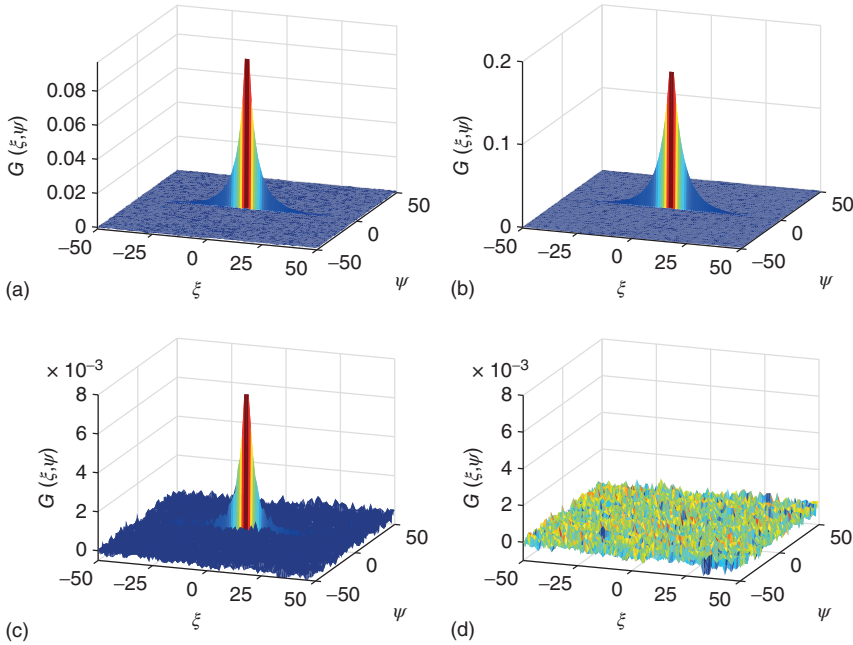


Figure 5.20 Influence of PIE on cross-correlation RICS. Raster-scanning images were collected for a solution of Atto488 and Atto565. The RICS autocorrelation function is shown for (a) Atto488 and (b) Atto565. As these dye molecules do not interact, there should be no residual cross-correlation. (c) The cross-correlation function is shown where the information available from PIE is not incorporated and all photons detected in the green channel are correlated with all photons detected in the red channel. (d) The same dataset is analyzed, but this time utilizing the PIE information to eliminate cross-talk. Here, the photons detected in the green channel after green excitation are correlated with photons detected in the red channel after red excitation. The residual cross-correlation due to spectral cross-talk is completely removed with PIE.

and s is the distance between contiguous pixels. The RICS ACF of DNA labeled with Atto565 freely diffusing in buffered solution is shown in Figure 5.19b. Here, the two different timescales become apparent: along the x -axis, the laser is scanned quickly and gives the width of the PSF unless the molecules diffuse more rapidly than the laser is scanned. Along the y -axis, more time passes before the laser beam returns to the same area. Fast moving particles will diffuse away, leading to a lower correlation amplitude at short distances but a higher probability of the particle being detected further away. For slowly diffusing molecules, the amplitude will be higher at short distances but decays to zero at distances larger than the PSF. For immobilized molecules that are much smaller than the size of the PSF, RICS returns the shape of the PSF. By fitting the RICS data with the theoretical expression for the ACF (Eq. (5.39)), the diffusion coefficient and average number of particles in the PSF can be determined. It is also possible to measure interactions using cross-correlation spectroscopy by performing RICS with two colors. Figure 5.20 shows the RICS ACF and CCF for two noninteracting fluorophores, Atto488 (Figure 5.20a) and Atto565 (Figure 5.20b), in solution. Figure 5.20c shows the RICS CCF without segregating the photons based on PIE. The spectral cross-talk of Atto448 into the Atto565 channel leads to a residual correlation, even though the particles do not interact. When taking the PIE information into account and correlating the photons detected in the green channel after green excitation with the photons detected in the red channel after red excitation, the residual cross-correlation completely disappears as shown in Figure 5.20d. Hence, as with FCCS, the sensitivity of two-color RICS experiments is enhanced with PIE. The applicability of RICS to cellular measurements can also be improved by a generalization of the ICS algorithm referred to as arbitrary region RICS (ARICS) [39]. The improved algorithm makes it possible to perform RICS on regions of interest of arbitrary shape that can be selected manually, automatically via thresholding or based on parameters measured in a second channel. Thus, ARICS enables measurements of diffusional motion within subcellular compartments.

Acknowledgments

We thank Dr Gregor Heiss, Dr Martin Sikor, Dr Adriano A. Torrano, Anders Barth, Nader Danaei, and Ivo Glück for measurements presented in this work. We gratefully acknowledge the financial support of the Deutsche Forschungsgemeinschaft through the Excellence Cluster Nanosystems Initiative Munich (NIM) and the Ludwig Maximilian University of Munich through the LMU Innovativ BioImaging Network (BIN) and the Center for NanoScience (CeNS).

References

- 1 Airy, G.B. (1835) On the diffraction of an object-glass with circular aperture. *Trans. Cambridge Philos. Soc.*, **5**, 283–291.
- 2 Abbé, E. (1873) Beiträge zur Theorie des Mikroskops und der mikroskopischen Wahrnehmung. *Arch. Mikrosk. Anat.*, **9**, 413–468.
- 3 Strutt, J.W. (1879) Investigations in optics, with special reference to the spectroscope. *Philos. Mag.*, **5**, 261–274.

- 4 Sparrow, C.M. (1916) On spectroscopic resolving power. *Astrophys. J.*, **44**, 76–86.
- 5 Minsky, M. (1961) Microscopy apparatus. US Patent 3013467, Dec. 19, 1961.
- 6 Naora, H. (1951) Microspectrophotometry and cytochemical analysis of nucleic acids. *Science*, **114** (2959), 279–280.
- 7 Minsky, M. (1988) Memoir on inventing the confocal scanning microscope. *Scanning*, **10**, 128–138.
- 8 Ploem, J.S. (1967) The use of a vertical illuminator with interchangeable dichroic mirrors for fluorescence microscopy with incident light. *Z. Wiss. Mikrosk.*, **68**, 129–142.
- 9 Egger, M.D. and Petran, M. (1967) New reflected-light microscope for viewing unstained brain and ganglion cells. *Science*, **157** (3786), 305–307.
- 10 White, J.G., Amos, W.B., and Fordham, M. (1987) An evaluation of confocal versus conventional imaging of biological structures by fluorescence light microscopy. *J. Cell Biol.*, **105** (1), 41–48.
- 11 van Meer, G., Stelzer, E.H.K., Wijnaendts-van-Resandt, R.W., and Simons, K. (1987) Sorting of sphingolipids in epithelial (Madin–Darby canine kidney) cells. *J. Cell Biol.*, **105** (4), 1623–1635.
- 12 Novotny, L. and Hecht, B. (2006) *Principles of Nano-Optics*, 1st edn, Cambridge University Press, Cambridge.
- 13 Webb, R.H. (1996) Confocal optical microscopy. *Rep. Prog. Phys.*, **59**, 427–471.
- 14 Wilhelm, S. (2008) *Confocal Laser Scanning Microscopy*, Carl Zeiss MicroImaging GmbH, Jena.
- 15 Jonkman, J.E.N. and Stelzer, E.H.K. (2001) in *Confocal and Two-Photon Microscopy: Foundations, Applications and Advances* (ed. A. Diaspro), Wiley-Liss Inc., New York, pp. 101–125.
- 16 Pawley, J.B. (2006) *Handbook of Biological Confocal Microscopy*, 3rd edn, Springer, New York.
- 17 Young, J.Z. and Roberts, F. (1951) A flying-spot microscope. *Nature*, **167** (4241), 231.
- 18 Nipkow, P. (1884) Elektrisches Teleskop. Germany Patent 30105, Jan. 15, 1885.
- 19 Richardson, W.H. (1972) Bayesian-based iterative method of image restoration. *J. Opt. Soc. Am.*, **62** (1), 55–59.
- 20 Haustein, E. and Schwille, P. (2007) Fluorescence correlation spectroscopy: novel variations of an established technique. *Annu. Rev. Biophys. Biomol. Struct.*, **36** (1), 151–169.
- 21 Lakowicz, J.R. (2006) *Principles of Fluorescence Spectroscopy*, 3rd edn, Springer, Berlin.
- 22 Lamb, D.C. (2009) in *Single Particle Tracking and Single Molecule Energy Transfer* (eds C. Bräuchle, D.C. Lamb, and J. Michaelis), Wiley-VCH Verlag GmbH, Weinheim, pp. 99–129.
- 23 Elson, E.L. and Magde, D. (1974) Fluorescence correlation spectroscopy. I. Conceptual basis and theory. *Biopolymers*, **13** (1), 1–27.
- 24 Magde, D., Elson, E., and Webb, W.W. (1972) Thermodynamic fluctuations in a reacting system: measurement by fluorescence correlation spectroscopy. *Phys. Rev. Lett.*, **29** (11), 705.

- 25 Rigler, R., Mets, Ü., Widengren, J., and Kask, P. (1993) Fluorescence correlation spectroscopy with high count rate and low background: analysis of translational diffusion. *Eur. Biophys. J.*, **22** (3), 169–175.
- 26 Macdonald, P., Johnson, J., Smith, E., Chen, Y., and Mueller, J.D. (2013) in *Methods in Enzymology: Fluorescence Fluctuation Spectroscopy (FFS)*, Part A, vol. **518** (ed. S.Y. Tetin), Elsevier, Oxford, pp. 71–98.
- 27 Schwille, P., Meyer-Almes, F.J., and Rigler, R. (1997) Dual-color fluorescence cross-correlation spectroscopy for multicomponent diffusional analysis in solution. *Biophys. J.*, **72** (4), 1878–1886.
- 28 Foo, Y.H., Naredi-Rainer, N., Lamb Don, C., Ahmed, S., and Wohland, T. (2012) Factors affecting the quantification of biomolecular interactions by fluorescence cross-correlation spectroscopy. *Biophys. J.*, **102** (5), 1174–1183.
- 29 Muller, B.K., Zaychikov, E., Brauchle, C., and Lamb, D.C. (2005) Pulsed interleaved excitation. *Biophys. J.*, **89** (5), 3508–3522.
- 30 Kapanidis, A.N., Lee, N.K., Laurence, T.A., Doose, S., Margeat, E., and Weiss, S. (2004) Fluorescence-aided molecule sorting: analysis of structure and interactions by alternating-laser excitation of single molecules. *Proc. Natl. Acad. Sci. U.S.A.*, **101** (24), 8936–8941.
- 31 Shera, E.B., Seitzinger, N.K., Davis, L.M., Keller, R.A., and Soper, S.A. (1990) Detection of single fluorescent molecules. *Chem. Phys. Lett.*, **174** (6), 553–557.
- 32 Zander, C., Sauer, M., Drexhage, K.H., Ko, D.S., Schulz, A., Wolfrum, J. *et al.* (1996) Detection and characterization of single molecules in aqueous solution. *Appl. Phys. B*, **63** (5), 517–523.
- 33 Widengren, J., Kudryavtsev, V., Antonik, M., Berger, S., Gerken, M., and Seidel, C.A.M. (2006) Single-molecule detection and identification of multiple species by multiparameter fluorescence detection. *Anal. Chem.*, **78** (6), 2039–2050.
- 34 Kudryavtsev, V., Sikor, M., Kalinin, S., Mokranjac, D., Seidel, C.A.M., and Lamb, D.C. (2012) Combining MFD and PIE for accurate single-pair Förster resonance energy transfer measurements. *ChemPhysChem*, **13** (4), 1060–1078.
- 35 Digman, M.A., Dalal, R., Horwitz, A.F., and Gratton, E. (2008) Mapping the number of molecules and brightness in the laser scanning microscope. *Biophys. J.*, **94** (6), 2320–2332.
- 36 Chen, Y., Müller, J.D., Ruan, Q., and Gratton, E. (2002) Molecular brightness characterization of EGFP in vivo by fluorescence fluctuation spectroscopy. *Biophys. J.*, **82** (1), 133–144.
- 37 Höller, M. (2011) *Advanced Fluorescence Fluctuation Spectroscopy with Pulsed Interleaved Excitation*, Ludwig-Maximilians Universität, Munich.
- 38 Digman, M.A., Sengupta, P., Wiseman, P.W., Brown, C.M., Horwitz, A.R., and Gratton, E. (2005) Fluctuation correlation spectroscopy with a laser-scanning microscope: exploiting the hidden time structure. *Biophys. J.*, **88** (5), L33–L36.
- 39 Hendrix, J., Dekens, T., Schrimpf, W., and Lamb, D.C. (2016). Arbitrary-Region Raster Image Correlation Spectroscopy. *Biophys. J.*, **111** (8), 1785–1796.